ADVANCED ELECTRONIC MATERIALS
Open Access
www.advelectronicmat.de

Experimental and Theoretical Studies of the Surface Oxidation Process of Rare-Earth Tritellurides

Jan Kopaczek, Kentaro Yumigeta, Akram Ibrahim, Mohammed Y. Sayyad, Shantanu Sinha, Renee Sailus, Patrick Hays, Seyed Tohid Rajaei Moosavy, Sandhya Susarla, Can Ataca,* Robert Kudrawiec, and Sefaattin Tongay**

Recent studies have established Van der Waals (vdW) layered and 2D rare-earth tritellurides (RTe_3) as superconductors and near room-temperature charge density wave (CDW) materials. Their environmental stability raises natural concern owing to aging/stability effects observed in other tellurium-based layered crystals. Here, the results establish the stability and environmental aging characteristics of these RTe_3 systems involving a variety of metals such as La, Nd, Sm, Gd, Dy, and Ho. The atomic force microscopy (AFM) and scanning electron microscopy (SEM) results show that all the RTe_3 sheets oxidize to form thin TeO_x layers that are primarily confined to the surface, edges, and grain boundaries. Time-resolved in situ Raman spectroscopy measurements are used to understand the kinetics of the oxidization process for different lanthanide metal cations and establish their relative stability/resilience to oxidization. Overall results indicate that the vdW layers show higher air stability as the *4f* electron number decreases going from Ho to La, resulting in the most stable $LaTe_3$ compared to the least stable $HoTe_3$. Comprehensive quantum mechanical simulations reveal that environmental degradation originates from a strong oxidizing reaction with O_2 molecules, while humidity (H_2O) plays a negligible role unless Te vacancies are present. Moreover, the simulations explain the effects of *4f* electrons on the work function and Te vacancies formation, which directly impact the aging characteristics of RTe_3 layers. Interestingly, optical and electrical measurements show that the CDW response is still observed in aged RTe_3 layers owing to the presence of underlying pristine/nonoxidized RTe_3 layers, except CDW transition temperatures increase due to the thickness effect. Overall results offer the first in-depth environmental aging studies on these materials, which can be applied to engineer and design their chemical stability, surface properties, and overall CDW characteristics.

1. Introduction

Van der Waals layered crystals that exhibit charge density waves (CDW) formation belong to a broad class of material systems with unique physical properties.[1–6] Superconductivity state,[1,7,8] temperature-induced Peierls dimerization,[9,10] and other exotic quantum phenomena[5] have been widely studied for these unique class of materials. One of the examples of this class of vdW CDW crystals is the lanthanide tritellurides series with the chemical formula of rare-earth tritellurides (RTe_3), where R stands for the rare-earth elements from La to Tm.[11] Previous studies have shown the emergence of temperature-driven CDW phase in RTe_3 based on Raman spectroscopy,[12,13] electrical resistivity measurements,[4,14] angle-resolved photoelectron spectroscopy (ARPES),[15,16] as well as electron diffraction.[17,18] The presence of the CDW state was attributed to the Fermi surface nesting or strong electron-phonon interaction and can be accompanied by the Kohn anomaly.[13,19,20] Overall, RTe_3 materials exhibit CDW phase transition temperature (T_{CDW}) ranging from below room temperature (220 K for $TmTe_3$) to well-above room temperature (550 K for $LaTe_3$) across the entire lanthanide series.[11,14]

J. Kopaczek, K. Yumigeta, M. Y. Sayyad, S. Sinha, R. Sailus, P. Hays, S. T. R. Moosavy, S. Susarla, S. Tongay
Materials Science and Engineering
School for Engineering of Matter
Transport and Energy
Arizona State University
Tempe, AZ 85287, USA
E-mail: jkopacze@asu.edu; sefaattin.tongay@asu.edu

The ORCID identification number(s) for the author(s) of this article can be found under https://doi.org/10.1002/aelm.202201129.

DOI: 10.1002/aelm.202201129

J. Kopaczek, R. Kudrawiec
Department of Semiconductor Materials Engineering
Faculty of Fundamental Problems of Technology
Wroclaw University of Science and Technology
Wybrzeże Wyspiańskiego 27, Wrocław 50–370, Poland

A. Ibrahim, C. Ataca
Department of Physics
University of Maryland-Baltimore County
Baltimore, MD 21250, USA
E-mail: ataca@umbc.edu

For practical applications of RTe_3 materials, however, their air stability plays a critical role that ultimately dictates the reliability and lifetime of the device. Because of their large surface-to-volume ratio, 2D materials and even vdW layered crystals raise concerns regarding their stability.[21–23] This is particularly true for tellurium-based material systems, including but not limited to tellurene, GaTe, Bi_2Te_3, InTe, and others.[22,24–27] While the physical properties of RTe_3 layers were extensively studied, their environmental stability remains at its seminal stages. Prior work has shown that high carrier mobility and antiferromagnetic $GdTe_3$ with T_{CDW} above room temperature (377 K)[28,29] should be more air-sensitive compared to early RTe_3 (toward $LaTe_3$),[30] which was claimed based on the visual observation of the change in crystal color. In general, more studies are needed to establish the environmental stability of RTe_3 materials using in situ techniques and understand the aging mechanism behind these degradation effects.

Here, we present comprehensive environmental degradation studies across the lanthanide tritellurides series from early to late RTe_3 compounds, namely, $LaTe_3$, $NdTe_3$, $SmTe_3$, $GdTe_3$, $DyTe_3$, and $HoTe_3$. Using optical and microscopy techniques, our studies establish the aging dynamics (kinetics) and the resilience to degradation when different RTe_3 materials are subjected to the same environmental conditions. In situ Raman spectroscopy studies show that there is a correlation between environmental aging time scales, metal cation atomic number, and *b* out-of-plane lattice constant (chemical pressure). At the same time, SEM and atomic force microscopy (AFM) techniques shed light on aging characteristics on the surface. Experimental findings are explained within the density functional theory (DFT) studies to reveal the chemical origin of degradation as well as the correlation between atomic numbers and the kinetics of the aging process.

2. Material Growth and Characteristics

In our studies, RTe_3 crystals were grown using the chemical vapor transport (CVT) or self-flux (flux) technique. $NdTe_3$, $SmTe_3$, $GdTe_3$, and $DyTe_3$ crystals were realized using the CVT technique from elemental precursors of metal lanthanide and tellurium powders (99.999%, Alfa Aesar).[31] The typical growth procedure involved sealing these precursors with 20 mg of iodine (I_2) as a transporting agent in a 2 mm thick quartz ampoule and subsequently pumping it down to pressure better than 10^{-5} Torr. Crystal growth was realized at 830 °C with ΔT = 10 °C thermal gradient for 1–2 weeks to produce millimeter to centimeter-sized crystals. $LaTe_3$ and $HoTe_3$ crystals were grown using a flux technique wherein the molar ratio R:Te = 3:97 mixture was kept in an alumina crucible under a vacuum. The quartz ampoule was heated to 700 °C within 8 h to create a mixture solute, and the ampoule was slowly cooled down to 515 °C at a rate of 2 °C min^{-1} to reject metal cations and to form the desired RTe_3 crystals. $LaTe_3$ and $HoTe_3$ were centrifuged to separate vdW crystal from Te liquid to collect crystals.

Typical growth procedure provided millimeter to centimeter-sized crystals, as shown in **Figure 1**a, which exhibit clear edges and a van der Waals nature. The energy-dispersive X-ray (EDS) results show that lanthanide-based metals and tellurium are distributed uniformly across van der Walls sheets without any phase separation, as shown in Figure 1c. Additionally, X-ray diffraction (XRD – obtained by the Malvern PANalytical Aeris system with CuKα radiation) confirmed the high crystallinity and layered nature of the studied crystals, as shown in Figure 1b. As the R lanthanide metal cation atomic number increases, the XRD reflection shifts to higher values, corresponding to lattice constant reduction (from 26.27 Å for $LaTe_3$ to 25.36 Å for $HoTe_3$). This behavior is related to the so-called lanthanide contraction effect, where the atomic radius decreases due to poorer shielding of *4f* orbital from the increased charge of atomic nuclei.[32] SEM (Zeiss Auriga FIB-SEM) for one of the freshly exfoliated lanthanide tritellurides material is shown in Figure 1d. The high crystallinity of the material can be evidenced by the 135° angles between the edges of the crystal sheet, which is related to its symmetry.

2.1. Microscopy Studies to Understand the Aging Effects

Tellurium-based layered vdWs material systems are widely studied as they exhibit different properties, such as single-photon emission,[33] the nonlinear effect,[34] magnetic order,[35] superconductivity,[36] and CDW state.[6] Previously it was shown that they could suffer from poor environmental stability,[27] and studies performed for GaTe provided information on the resilience of that material to different gases exposure.[22] That issue raises a question about the stability of the RTe_3 series, which hosts the CDW state within the Te atoms sheet enclosed by the RTe slab. That CDW state is formed along the *c*-axis, and for selected compounds, namely $TmTe_3$, $ErTe_3$, $HoTe_3$, and $DyTe_3$, below a specific temperature (in the range from 52 to 180 K), a second CDW along the a-axis is displayed.[14]

AFM and Kelvin probe force microscopy (KPFM) measurements were performed on RTe_3 crystal immediately after exfoliation (before oxidization **Figure 2**a,b) and after subjecting the same sheets (thickness = 20 nm) to air for 24 h in ambient conditions (after oxidization Figure 2d,e). Here, we note that the results in Figures 2,3 primarily focus on R = La owing to their higher air stability, allowing us to demonstrate aging effects across longer periods of time, which will be discussed in greater detail in later sections. AFM studies show that the air-exposed samples produce rough surfaces (Figure 2b) while the work function of the $LaTe_3$ increases from 4.700 ± 0.025 to 4.735 ± 0.025 eV as per KPFM surface analysis (the approach of work function estimation is described in Section S2.1, Supporting Information). Despite being small, the increase of the work function is uniform across the measured crystal which can be related to the formation of the oxide layer on its surface. To provide further information on the surface topography changes, vdW $LaTe_3$ was imaged under in situ SEM, as shown in Figure 2c,f. Before aging, vdW crystals show clear edges and terraces, as depicted in Figure 2c. Once the aging takes place, nanoparticle-like features appear on the surface, at the crystal edges, as well as at the terraces edge sites, which are visible in SEM images as well as oxygen atoms in EDS maps (inset Figure 2f). This behavior can be attributed to the higher chemical reactivity at the edges and terraces due to unpassivated/open chemical bonds lowering the chemical barrier for

ADVANCED ELECTRONIC MATERIALS
Open Access
www.advelectronicmat.de

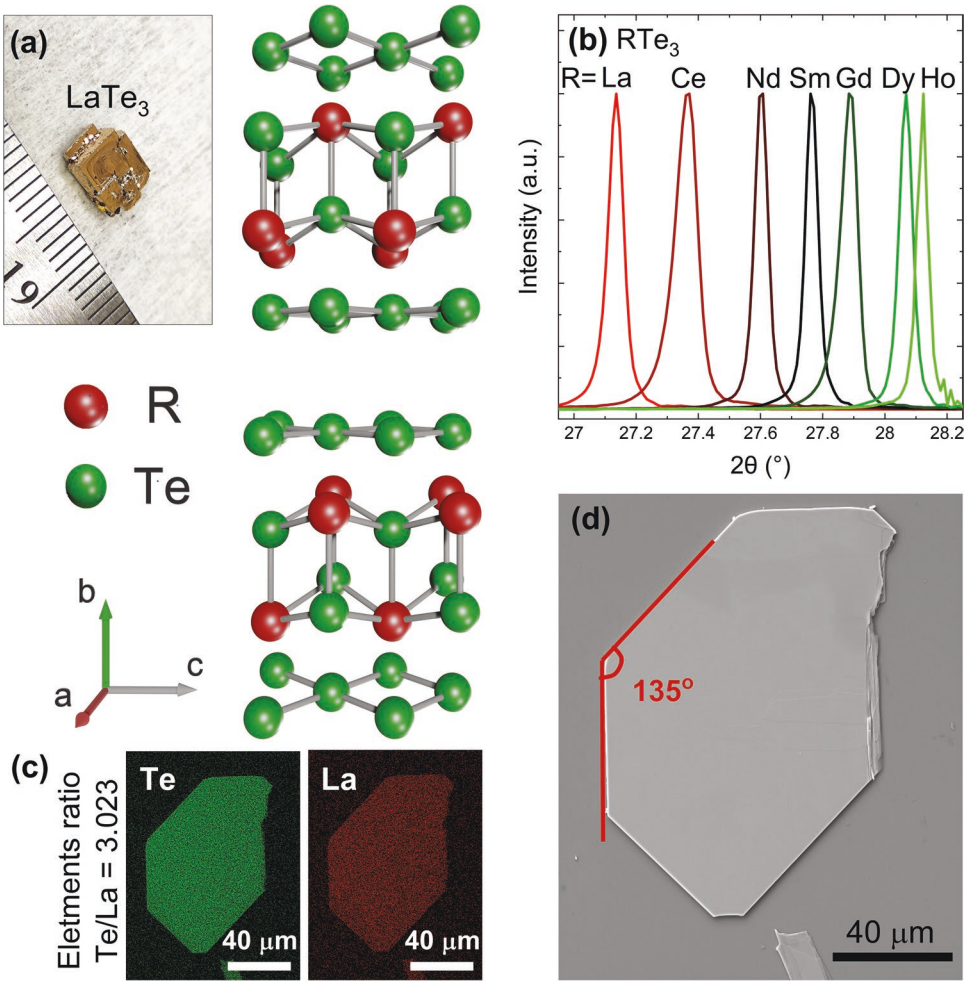

Figure 1. Characterization of a crystal structure for studied in this work rare-earth tritellurides (RTe_3) material systems. a) Exemplary optical image of millimeter size $LaTe_3$ crystal together with schematics of its unit cell. b) (080) X-ray diffraction (XRD) reflection for all studied here materials. c) Energy-dispersive X-ray (EDS) maps showing the spatial distribution of La and Te elements across that sample (1:3 stochiometric ratio is confirmed), and d) scanning electron microscopy (SEM) image for thin $LaTe_3$ crystal.

oxidization. While crystal surfaces show more resilience to oxidation than the edges, the surface still undergoes substantial environmental degradation after 1 day of exposure. Moreover, the formation of the oxide layer was confirmed unambiguously by XPS measurements performed for pristine and aged $DyTe_3$ crystals. These results, described in Section S2.2 (Supporting Information), show the emergence of new peaks related to Te oxide complexes.

2.2. In Situ Raman Spectroscopy and Kinetics of the Reaction

Time-dependent (in situ) Raman spectroscopy measurements were performed within a ≈2 months period in the backscattering configuration (with the use of CW 632 nm laser line) using 50× Mitutoyo objective with ≈5 μm spatial resolution. While collecting spectra, to avoid laser induce degradation in the presence of water molecules,[22] the crystals were kept under a vacuum (10^{-3} Torr) in a Linkam chamber. Here in **Figure 3**a, freshly exfoliated $LaTe_3$ sheets exhibit three prominent optical modes located at 88, 97, and 105 cm^{-1}, whereas the low-frequency Raman peak (amplitude mode at 70 cm^{-1}) is related to the CDW phase since $LaTe_3$ forms that phase at room temperature.[12,31] In situ Raman measurements show that 10 days after preparing fresh thin crystal by exfoliation, new peaks start to emerge at around 128 and 145 cm^{-1}. At the same time fundamental optical modes and CDW amplitude mode gradually reduce in Raman intensity across ≈2 months. A 2D contour plot constructed from the raw data (Figure 3a) is shown in Figure 3b to illustrate better the environmental degradation, which shows a clear transition from fundamental Raman modes to new emergent modes related to oxidation of the studied material. These emergent peaks exhibit much larger full-width-at-half-max (FWHM) than fundamental modes, suggesting that these oxide-based regions are disordered/amorphous in nature. Previous studies have shown that these modes at 130 and 145 cm^{-1} correspond to tellurium oxide complexes TeO_{2-x} arising primarily from the interaction between $H_2O_{(g)}$ and tellurium.[22]

To understand the kinetics of the oxidization reaction qualitatively, we have analyzed the ratio of integrated intensity between

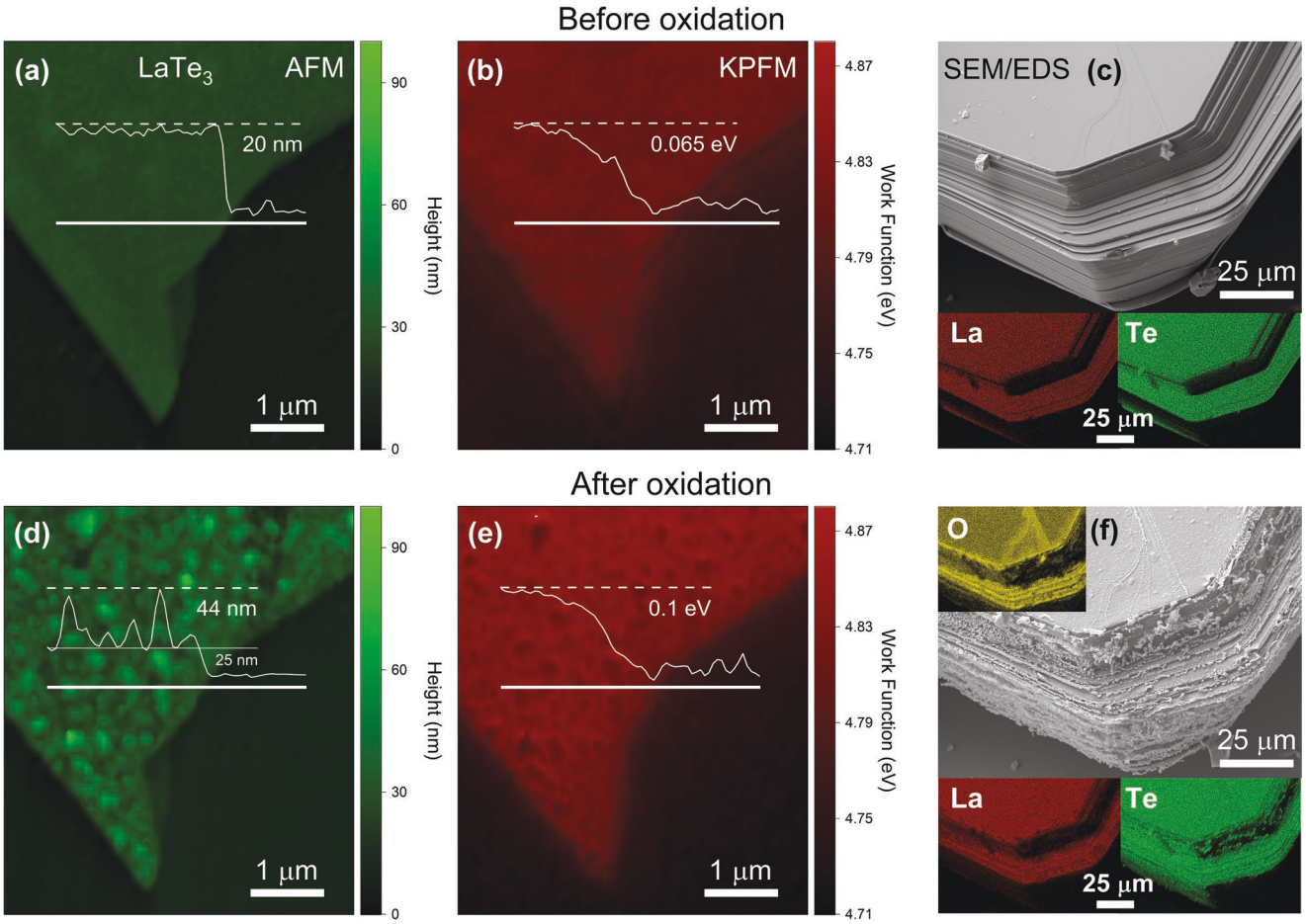

Figure 2. Surface characterization of $LaTe_3$ material. a) Atomic force microscopy (AFM), b) Kelvin probe force microscopy (KPFM) image, c) scanning electron microscopy (SEM) image/energy-dispersive X-ray (EDS) compositional maps before oxidation, and d–f) images after oxidation took place. AFM and KPFM scans were taken for thin crystal, whereas SEM/EDS measurements were performed for thick material, clearly showing its layered structure.

$LaTe_3$ (88 cm^{-1}) and TeO_x (128 cm^{-1}) Raman peaks. Since the intensity of the individual Raman modes is linearly proportional to the material quantity, the calculated time-dependent intensity ratio of $LaTe_3/TeO_x$ denotes the ability of a material to resist oxidization. The Raman intensity ratio of $LaTe_3/TeO_x$ (Figure 3c) shows that this integrated intensity ratio decreases with time, suggesting that the TeO_x peaks start to form from the $LaTe_3$ material. The observed response can be fitted to exponential decay. Such behavior is understood within the Deal–Grove model as the thickness of the oxide layer will form linearly but slow down in the diffusion-limited formation regime.[37] As such, the significant portion of the initial drop in the $LaTe_3/TeO_x$ ratio is ultimately followed by slow saturation as the formed TeO_x layer acts as a diffusion barrier, much similar to the oxidization process in silicon or other oxidizing material systems. Here we find that the half-life time equals 9 days, meaning the material-related Raman signal loses its original intensity by half.

2.3. In Situ Measurements in Other RTe3 Systems

Using a similar approach, we have extended our studies across the lanthanide tritellurides series, including $NdTe_3$, $SmTe_3$, $GdTe_3$, $DyTe_3$, and $HoTe_3$ (mentioned results are provided in Section S2.3, Supporting Information). These measurements were repeated on a large number of samples (+20) for a better statistical representation of the oxidization characteristics. The results (**Figure 4**) reveal that $DyTe_3$ and $HoTe_3$ have very small resilience to oxidization, meaning they readily oxidize when exposed to ambient conditions, as obtained by the half-time oxidization analysis presented for $LaTe_3$ in Figure 3c. In contrast, $NdTe_3$, $SmTe_3$, and $GdTe_3$ exhibit moderate resilience to oxidization with half-time oxidization characteristics ranging from 2 to 6 days for $GdTe_3$ and $NdTe_3$, respectively. Whereas, $LaTe_3$ has the highest durability to aging transformation (for that reason, our previous Figures show results obtained for $LaTe_3$ material, which allows detailed analysis of the kinetics of the reaction). Overall findings summarized in Figure 4 clearly indicate a strong relationship between oxidization and the 4*f* electron number. Since the out-of-plane lattice constant (*b*) is smaller (also in-plane (*a*) and (*c*) lattice constants reduced) for increasing 4*f* electron number (see Figure 1b), similar conclusions can be drawn for oxidation tendency and lattice constant (*b*) (Figure 4 inset). A detailed explanation of the nature of the oxidation phenomenon is provided in the following section.

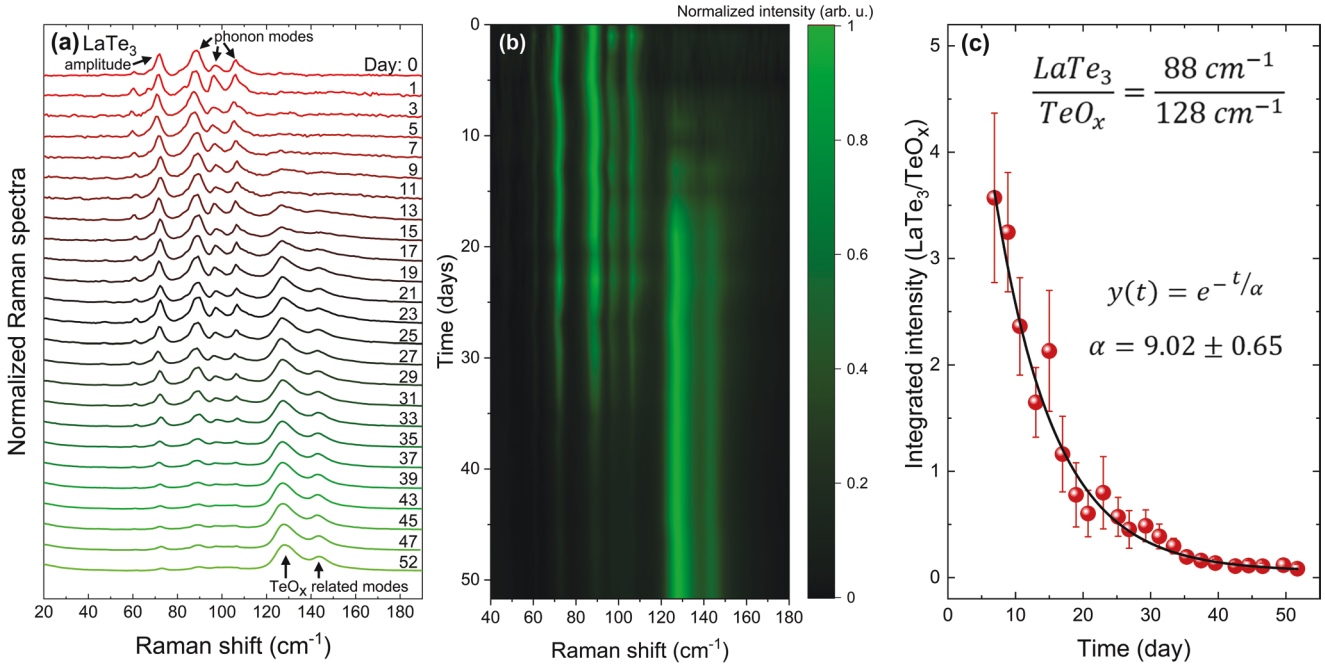

Figure 3. Time-dependent Raman studies of the kinetics of oxidation of $LaTe_3$ material. a) Raman spectra of $LaTe_3$ crystal were obtained as time progressed from 0 to 52 days. b) 2D contour plot of spectra from graph (a). c) The time-dependent ratio of the integrated intensity of one of the $LaTe_3$ vibrational modes (88 cm^{-1}) and TeO_x (128 cm^{-1}) oxidation peaks. The black line represents fitting with an exponential function.

2.4. Theoretical Insights into Oxidation Reactions and Environmental Stability

DFT simulations were carried out to unravel the origin of the observed oxidation resilience trend and provide insight into the oxidation mechanisms of RTe_3 materials. To explain the origin of the resilience trend, we also performed DFT calculations of the work function (Φ) for pristine RTe_3 crystal. In general, a higher Φ should refer to a higher energy barrier that the oxidant needs to overcome in order to capture electrons from the surface of the material to form a chemical bond, which should translate into a higher oxidation resilience. In Figure 4b, we show a plot of Φ values calculated for monolayers of the different RTe_3 materials considered in this study. The plot indeed exhibits a trend of Φ with *4f* electrons similar to the oxidation resilience trend. This behavior of Φ can be attributed to the poor shielding effect of *4f* electrons, which leads to a greater effective attraction of electrons by the nucleus as the number of *4f* electrons increases.[38,39] This results in a decrease in the atomic radius which is manifested by smaller lattice parameters (Figure 4a, Figure S2, Supporting Information), as well as an increase in the electronegativity of the lanthanide atom with the increase in the number of *4f* electrons. In turn, a smaller electronegativity difference between R and Te atoms results in a weaker chemical bonding, making it easier for the oxidant to capture electrons from the surface of RTe_3. This weaker

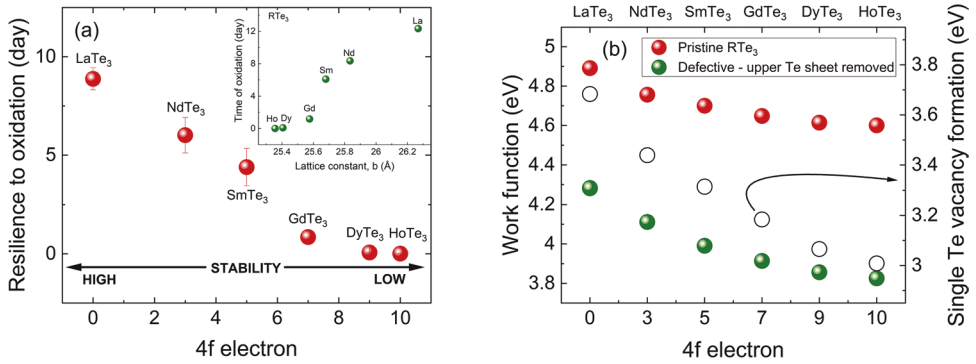

Figure 4. Resilience/stability to oxidation across rare-earth tritellurides (RTe_3) material systems. a) Resilience to oxidation in the function of *4f* electron number for studied here crystals, inset graph shows the relation between out of plane (*b*) lattice constant and half-time of oxidation. b) Calculated dependence of work function versus *4f* electron number for pristine and defective RTe_3 crystal and also dependence for single Te vacancy formation (right axis in the figure).

ADVANCED ELECTRONIC MATERIALS
Open Access
www.advelectronicmat.de

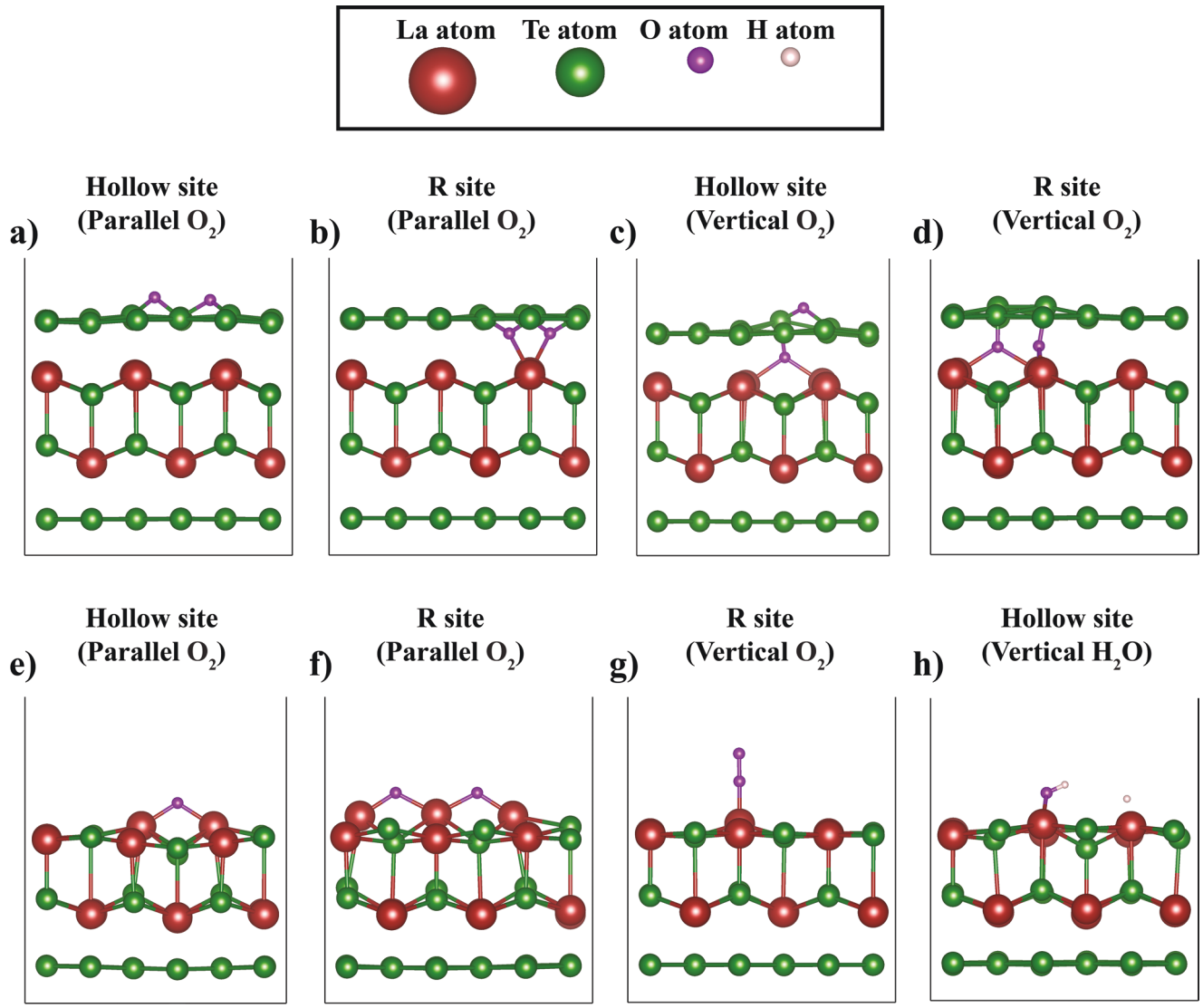

Figure 5. Equilibrium configurations of the oxidized pristine rare-earth tritellurides (RTe_3) (upper row) and the defective RTe_3 with the upper Te sheet removed (lower row), as obtained by density functional theory (DFT). The titles of subfigures refer to different expected oxidants (O_2/H_2O) along with their potential initial adsorption site (R/hollow sites) and orientation (parallel/vertical) with respect to the RTe_3 monolayer.

bonding is evinced by a decrease in the cohesive energy of RTe_3 materials with the increase in the number of *4f* electrons (Figure S3a, Supporting Information).

Furthermore, to determine the types of gas molecules responsible for the strong surface interaction, DFT simulations were performed to investigate the reactivity of both H_2O and O_2 on top of clean $LaTe_3$ and $HoTe_3$ sheets. The adsorption of both molecules is examined on top of $3 \times 1 \times 3$ supercells at three high symmetry sites (Te, R, and hollow sites) with two possible orientations (parallel and vertical) with respect to the monolayer as illustrated in Figure S1 (Supporting Information). Considering a pristine monolayer of RTe_3, independent from the potential, three binding sites and how close H_2O molecules interact with the RTe_3 surfaces, H_2O molecules did not dissociate instead only remained in their physisorption state (see Section (d), Supporting Information). This implies a substantially high dissociation barrier and excludes H_2O (humidity) as one of the aging catalysts for pristine RTe_3. On the contrary, oxygen molecules exhibited strong dissociative chemisorption, as shown in **Figure 5**. The upper row of Figure 5 depicts four distinct equilibrium configurations that resulted from exothermic O_2 chemical adsorption on pristine $LaTe_3$ and $HoTe_3$. **Table 1** outlines the binding energies, bond lengths, and charge transfer for these configurations. From Table 1, we can first observe that for (b), (c), and (d) configurations, the binding energies are always stronger for $HoTe_3$, which originates from the shorter average bond lengths between oxygen atoms and their nearest neighbor Ho atoms caused by the poor shielding of *4f* electrons. Second, the charge transfer to oxygen atoms is approximately identical for both $LaTe_3$ and $HoTe_3$ in all configurations due to the fact that *4f* electrons have limited radial extension and thus are not contributing to charge transfer and bond formation. For configuration (a), where oxygen atoms bind to the upper side of the Te sheet, we can generally observe

Table 1. Binding energies (E_{bind}), charge transfer to the oxidant (ΔQ), and average bond length between O atoms and their nearest neighbor R atoms ($d_{O\text{-}R}$) are outlined for the four configurations identified for O_2 chemisorption on top of pristine $LaTe_3$ and $HoTe_3$.

Oxidizer (site and orientation)	E_{bind} [eV]		ΔQ [e$^-$]		$d_{O\text{-}R}$ [Å]	
	$LaTe_3$	$HoTe_3$	$LaTe_3$	$HoTe_3$	$LaTe_3$	$HoTe_3$
a) O_2 (Hollow site – parallel)	−1.02	−1.02	2.04	2.03	3.91	4.18
b) O_2 (Hollow site – vertical)	−3.43	−3.71	2.24	2.34	2.40	2.31
c) O_2 (R site – parallel)	−2.56	−2.58	2.22	2.24	2.38	2.27
d) O_2 (R site – vertical)	−4.36	−4.79	2.37	2.34	2.38	2.26

smaller binding energies ascribed to the smaller electronegativity difference between O and Te compared to O and R. In addition, the binding energies of oxygen atoms in configuration (a) are equal and independent of their average distance from the nearest neighbor lanthanide atoms, which demonstrates the short-sightedness of the *4f* electrons, meaning that the influence of *4f* electrons on the binding characteristics can be considered negligible unless oxygen atoms bind directly to R atoms. This behavior agrees with the observed very small difference in physisorption energies (≈0.015 eV lower for $HoTe_3$) (Table S3, Supporting Information), as well as the nearly equal energies (≈0.01 eV difference) of dissociation transition states of O_2 above $LaTe_3$ and $HoTe_3$ (see Section (f), Supporting Information). From these observations, we can infer that O_2 on top of $HoTe_3$ would exhibit (1) slightly more stable physisorption states, leading to a higher number of trial attempts for crossing the dissociation barrier and getting chemisorbed, (2) relatively more stable chemisorption states, and thus a lower rate of oxygen desorption from the surface, leading to faster aging. This generally indicates the higher reactivity of RTe_3 materials to oxygen as the number of *4f* electrons increases, as observed from the experimental results and predicted as well by the work function calculations. Sections (e)-(f) (Supporting Information) include detail of our simulations of O_2 adsorption on RTe_3.

From the pristine configurations in Figure 5, we can notice the higher tendency of oxygen atoms to diffuse under the Te sheets to bind to lanthanide atoms. Moreover, for cases where oxygen binds to the upper side of the Te sheet, such as in configuration (a), we observe identical binding energies (Table 1), and accordingly, one would expect similar aging behavior of different RTe_3, which is contradictory to the experimental observations. This, in general, promotes the idea that the observed resilience trend originates from a dominant direct binding of the oxidant atoms to lanthanide atoms. Furthermore, the fast oxidation of RTe_3 materials observed in water (shown in Figure S20, Supporting Information), along with the DFT results showing relatively high dissociation barriers of H_2O above pristine RTe_3 monolayers, suggest that H_2O molecules could interact with RTe_3 if they have the opportunity to diffuse more easily under the Te sheets and directly interact with lanthanide atoms. This can be related to the influence of Te vacancy defects (V_{Te}) on reactivity. To investigate this, we performed DFT simulations of defected $LaTe_3$ and $HoTe_3$ monolayers where the upper tellurium sheet is completely removed. Although a full removal of the upper Te sheet might appear as a severe assumption, it helps to investigate the behavior of surface spots that have multiple V_{Te} where O_2 or H_2O molecules get the opportunity to interact directly with the inner R atoms. The lower row of Figure 5 depicts the distinct configurations with exothermic adsorption reactions, while **Table 2** outlines their characteristics. From Table 2, we can observe consistent behaviors of roughly equal charge transfers, along with shorter bonds and stronger binding energies for $HoTe_3$. Second, the oxygen binding energies are noticed to be three to five times stronger compared to the pristine RTe_3 model.

This can indicate the role played by the upper Te sheet as a protective barrier against environmental aging. The obtained stronger binding energies further agree with the reductions observed in the work function after removing the upper Te sheet (Figure 4b). Interestingly, we can now observe H_2O dissociative chemisorption (configuration (h) in Figure 5), which indicates that the dissociation barrier for H_2O becomes finite after the removal of the upper Te sheet, promoting its interaction with RTe_3 materials. These results suggest that V_{Te} might be playing a vital role in determining the overall environmental stability characteristics of these material systems. In this retrospect, we calculated the Te vacancy formation energies of all RTe_3 materials considered in this work. Figure 4b (open black circle) shows that the formation energy of V_{Te} decreases with the number of *4f* electrons, which is an expected behavior

Table 2. Binding energies (E_{bind}), charge transfer to the oxidant (ΔQ), and average bond length between O atoms and their nearest neighbor R atoms ($d_{O\text{-}R}$) are outlined for the four configurations identified for O_2 chemisorption on top of defective $LaTe_3$ and $HoTe_3$ (after the removal of the upper tellurium sheet).

Oxidizer (site and orientation)	E_{bind} [eV]		ΔQ [e$^-$]		$d_{O\text{-}R}$ [Å]	
	$LaTe_3$	$HoTe_3$	$LaTe_3$	$HoTe_3$	$LaTe_3$	$HoTe_3$
e) O_2 (Hollow site – parallel)	−11.89	−11.97	2.41	2.41	2.15	2.06
f) O_2 (R site – parallel)	−11.95	−12.13	2.43	2.46	2.16	2.06
g) O_2 (R site – vertical)	−2.73	−3.03	0.98	0.94	2.75	2.64
h) H_2O (Hollow site – vertical)	−3.64	−3.93	1.36	1.35	2.44	2.31

considering the similar behavior of RTe_3 cohesive energies (Figure S3, Supporting Information). This point establishes V_{Te} formation as an extra factor contributing to the observed resilience trend, in addition to the role played by the work function. As the number of *4f* electrons increases, the RTe_3 material has a higher probability of the V_{Te} formation due to its lower formation energy, which results in much faster oxidation due to the higher binding energies of O_2 and H_2O to the inner R-Te slab. Overall, although *4f* electrons do not directly contribute to chemical bonding, their effects on the work function and the vacancy formation energy can still strongly affect the binding characteristics and the overall environmental stability of the material. More details about the DFT simulations, including binding energies, dissociation barriers, charge transfer, and structure optimization schemes for physisorption and chemisorption situations for both pristine and defected structures, are outlined in the Supporting Information file.

2.5. Effect of Oxidization on the CDW Characteristics

After discussing the origin of the aging effect, additional temperature-dependent Raman spectroscopy studies were carried out to understand how the environmental aging effect influences CDW formation. Here, $DyTe_3$ layers are ideal material testbed systems owing to their relatively fast oxidation characteristics as well as above liquid nitrogen CDW temperature allowing temperature-dependent Raman measurements to capture clean CDW transitions. Freshly exfoliated $DyTe_3$ sheets were subjected to continuous air exposure for 12 h, and temperature-dependent Raman measurements were performed on pristine (as-exfoliated) as well as aged $DyTe_3$ sheets, to assess the CDW behavior, as shown in **Figure 6**a,b, respectively.

Previously, the temperature variation of Raman modes was obtained by several authors to track the anti-crossing interaction between coupled phonon and amplitude mode and to determine the T_{CDW}.[12,31,40] As shown in Figure 6c, such anti-crossing behavior was observed for both pristine and aged $DyTe_3$ samples, where the frequency of CDW amplitude (at 68 cm^{-1}) and phonon (at 55 cm^{-1}) mode reduces as temperature increases starting from 80 K. Subsequently, at around 140 K **nature of both branches changes, and the top one is more phononic, whereas the bottom resembles amplitude mode. It can be seen that amplitude mode softens much quicker compared to phonon mode since the temperature diminishes the CDW order abruptly. At the same time, the temperature does not significantly affect the frequency of phonon mode as mainly related to the thermal expansion of the lattice. Comparison between oxidized and nonoxidized samples shows that this CDW amplitude and phonon cross-over regime remains similar. Moreover, based on the Ginzburg–Landau model, the extracted T_{CDW} values remain close for both samples (308 ± 5 K before and 312 ± 7 K after oxidation). These results suggest that the oxidation process is primarily a surface-limited reaction and oxidized surface ultimately prevent further oxidization from taking place. The formation on the surface of the oxide layer was shown by AFM and SEM/EDS measurements in Figure 2, while it can be seen in Figure 3c, that initial quick drop in the ratio of $LaTe_3/TeO_x$ mode intensity is followed by slow saturation. Such behavior supports the idea of oxidation happening from the surface. Moreover, the surface oxidization leaves an oxidized surface in conjunction with the nonoxidized regions within the exfoliated flakes. While the oxidized amorphous surface offers smaller Raman signals, the underlying RTe_3 layers remain intact and produce CDW Raman behavior, as observed in Figure 6b,c.

This was further confirmed by electrical resistivity measurements shown in Figure 6c inset. Pristine and aged $DyTe_3$ sheets still exhibit signature CDW behavior (Figure 6c inset), except the CDW transition temperature increases by about ≈20 ± 5 K as the RTe_3 layers get oxidized or the active pristine RTe_3 thickness is reduced. Here, an aging-induced increase in T_{CDW} can

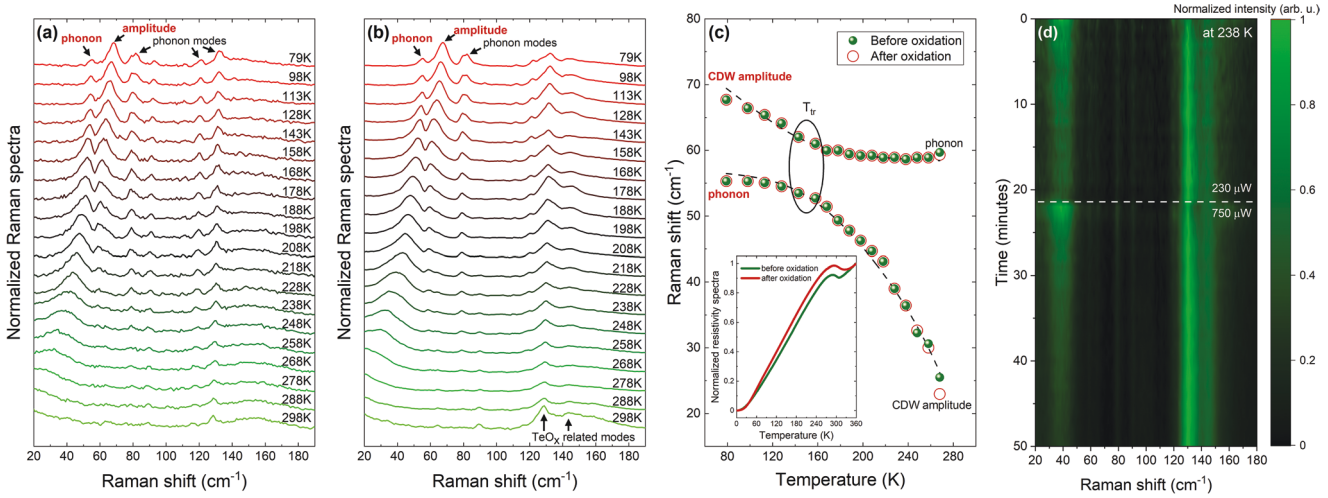

Figure 6. Studies of T_{CDW} after oxidation of $DyTe_3$ material, i.e., rare-earth tritellurides (RTe_3) compound for which T_{CDW} transition is around room temperature. a,b) Temperature-dependent Raman spectra before and after oxidation of the studied sample. c) Raman shift in the function of the temperature for charge density wave (CDW) amplitude and phonon mode (label of which is in red in panels (a) and (b)), inset graph shows normalized resistivity spectra obtained before/after oxidation. d) 2D contour plot of Raman spectra obtained at 238 K with time; shows how insensitive to oxidation is CDW amplitude mode (at ≈35 cm^{-1}). After 22 min, the laser power was increased to accelerate the oxidation process.

be attributed to the reduced thickness of nonoxidized RTe_3 as demonstrated for the $GdTe_3$[40] and $TiSe_2$[9] in which the T_{CDW} was found to be increasing for thinner CDW materials. Our results show full agreement with these studies and suggest that electrical current mainly probes the nonoxidized electrically conductive CDW portion of the $DyTe_3$ sheets while bypassing the oxidized TeO_x portion of the material or contributing to increased resistivity as observed in our samples (Figure 6c inset red-solid line). It is also noteworthy to mention that optical Raman spectroscopy measurements also show a slight increase in T_{CDW} values by ≈4K (Figure 6a,b), this effect falls within the error bar in our measurements due to the spectral resolution of the CDW amplitude modes (0.5 cm^{-1}) and inherently large FWHM values and low intensity count of the CDW amplitude modes presenting increased difficulties in assigning T_{CDW} values.

3. Conclusion

Comprehensive in situ Raman studies were carried out on van der Waals charge density wave RTe_3 lanthanide tritelluride materials to establish their oxidization characteristics, stability, and elucidate the origin of oxidization effects. Results show that the material stability increases as the 4*f* electrons are depleted or going from R = Ho → La. Computational studies show that O_2 molecules are the primary catalysts for the oxidization while humidity (H_2O) plays a negligible role, unless Te vacancies are present, in the environmental surface transformation process. Moreover, we propose an explanation based on the electronegativity of the R lanthanide cation element to provide a simple scheme of the observed experimental dependency of resilience to oxidation versus *4f* electron number. Due to the higher electronegativity of the late rare-earth lanthanides (i.e., Ho, Dy) compared to early ones (e.g., La, Nd), the electron cloud is pulled from the Te anion toward the R cation. That shift of the electron cloud away from the Te atom leads to weaker attraction with tellurium and makes the transfer of electrons from tellurium to oxygen easier. Detailed microscopy and spectroscopy measurements show that all the RTe_3 systems eventually oxidize to form thin TeO_x layers at the edges, terraces, and on the surface. However, a significant portion of the pristine material still resists oxidization due to the diffusion barrier created by the thin amorphous TeO_x surface layers. Aged materials still exhibit characteristics of CDW response except for their CDW transition temperatures which increase potentially due to reduced CDW material thickness after aging induced oxidization effect. The results on the oxidization kinetics and aging-induced changes in RTe_3 CDW behavior offer the first environmental aging insights into these material systems, which can be applied to engineer and design their chemical stability, surface properties, and overall CDW characteristics.

Supporting Information

Supporting Information is available from the Wiley Online Library or from the author.

Acknowledgements

S.T. acknowledges support from DOE-SC0020653, Applied Materials Inc., NSF CMMI 1825594, NSF DMR-1955889, NSF CMMI-1933214, NSF DMR-1904716, NSF 1935994, NSF ECCS 2052527, and DMR 2111812. The authors acknowledge the use of facilities within the Eyring Materials Center at Arizona State University and the ASU research computing center. J.K. acknowledges support within the Bekker program from the Polish National Agency for Academic Exchange. C.A. acknowledges support from NSF DMR-2213398.

Conflict of Interest

The authors declare no conflict of interest.

Data Availability Statement

The data that support the findings of this study are available from the corresponding author upon reasonable request.

Keywords

charge density waves (CDW), density functional theory (DFT) theory simulations, environmental stability, rare-earth tritellurides (RTe_3)

Received: October 10, 2022
Revised: January 18, 2023
Published online: February 28, 2023

[1] J. Chang, E. Blackburn, A. T. Holmes, N. B. Christensen, J. Larsen, J. Mesot, R. Liang, D. A. Bonn, W. N. Hardy, A. Watenphul, M. v. Zimmermann, E. M. Forgan, S. M. Hayden, *Nat. Phys.* **2012**, *8*, 871.
[2] Y. I. Joe, X. M. Chen, P. Ghaemi, K. D. Finkelstein, G. A. de la Peña, Y. Gan, J. C. T. Lee, S. Yuan, J. Geck, G. J. MacDougall, T. C. Chiang, S. L. Cooper, E. Fradkin, P. Abbamonte, *Nat. Phys.* **2014**, *10*, 421.
[3] X. Xi, L. Zhao, Z. Wang, H. Berger, L. Forró, J. Shan, K. F. Mak, *Nat. Nanotechnol.* **2015**, *10*, 765.
[4] D. A. Zocco, J. J. Hamlin, K. Grube, J.-H. Chu, H.-H. Kuo, I. R. Fisher, M. B. Maple, *Phys. Rev. B* **2015**, *91*, 205114.
[5] Y. Nakata, K. Sugawara, R. Shimizu, Y. Okada, P. Han, T. Hitosugi, K. Ueno, T. Sato, T. Takahashi, *NPG Asia Mater.* **2016**, *8*, e321.
[6] A. Kogar, A. Zong, P. E. Dolgirev, X. Shen, J. Straquadine, Y.-Q. Bie, X. Wang, T. Rohwer, I.-C. Tung, Y. Yang, R. Li, J. Yang, S. Weathersby, S. Park, M. E. Kozina, E. J. Sie, H. Wen, P. Jarillo-Herrero, I. R. Fisher, X. Wang, N. Gedik, *Nat. Phys.* **2020**, *16*, 159.
[7] E. Navarro-Moratalla, J. O. Island, S. Mañas-Valero, E. Pinilla-Cienfuegos, A. Castellanos-Gomez, J. Quereda, G. Rubio-Bollinger, L. Chirolli, J. A. Silva-Guillén, N. Agraït, G. A. Steele, F. Guinea, H. S. J. van der Zant, E. Coronado, *Nat. Commun.* **2016**, *7*, 11043.
[8] J. J. Hamlin, D. A. Zocco, T. A. Sayles, M. B. Maple, J.-H. Chu, I. R. Fisher, *Phys. Rev. Lett.* **2009**, *102*, 177002.
[9] P. Goli, J. Khan, D. Wickramaratne, R. K. Lake, A. A. Balandin, *Nano Lett.* **2012**, *12*, 5941.
[10] K. Rossnagel, *J. Phys.: Condens. Matter* **2011**, *23*, 213001.
[11] K. Yumigeta, Y. Qin, H. Li, M. Blei, Y. Attarde, C. Kopas, S. Tongay, *Adv. Sci.* **2021**, *8*, 2004762.
[12] M. Lavagnini, H.-M. Eiter, L. Tassini, B. Muschler, R. Hackl, R. Monnier, J.-H. Chu, I. R. Fisher, L. Degiorgi, *Phys. Rev. B* **2010**, *81*, 081101.

[13] M. Lavagnini, M. Baldini, A. Sacchetti, D. Di Castro, B. Delley, R. Monnier, J.-H. Chu, N. Ru, I. R. Fisher, P. Postorino, L. Degiorgi, *Phys. Rev. B* **2008**, *78*, 201101.
[14] N. Ru, C. L. Condron, G. Y. Margulis, K. Y. Shin, J. Laverock, S. B. Dugdale, M. F. Toney, I. R. Fisher, *Phys. Rev. B* **2008**, *77*, 035114.
[15] G.-H. Gweon, J. D. Denlinger, J. A. Clack, J. W. Allen, C. G. Olson, E. DiMasi, M. C. Aronson, B. Foran, S. Lee, *Phys. Rev. Lett.* **1998**, *81*, 886.
[16] V. Brouet, W. L. Yang, X. J. Zhou, Z. Hussain, N. Ru, K. Y. Shin, I. R. Fisher, Z. X. Shen, *Phys. Rev. Lett.* **2004**, *93*, 126405.
[17] E. DiMasi, M. C. Aronson, J. F. Mansfield, B. Foran, S. Lee, *Phys. Rev. B* **1995**, *52*, 14516.
[18] C. Malliakas, S. J. L. Billinge, H. J. Kim, M. G. Kanatzidis, *J. Am. Chem. Soc.* **2005**, *127*, 6510.
[19] M. D. Johannes, I. I. Mazin, *Phys. Rev. B* **2008**, *77*, 165135.
[20] N. Lazarević, Z. V. Popović, R. Hu, C. Petrovic, *Phys. Rev. B* **2011**, *83*, 024302.
[21] X. Wang, Y. Sun, K. Liu, *2D Mater.* **2019**, *6*, 042001.
[22] S. Yang, H. Cai, B. Chen, C. Ko, V. O. Özçelik, D. F. Ogletree, C. E. White, Y. Shen, S. Tongay, *Nanoscale* **2017**, *9*, 12288.
[23] S. Ahn, G. Kim, P. K. Nayak, S. I. Yoon, H. Lim, H.-J. Shin, H. S. Shin, *ACS Nano* **2016**, *10*, 8973.
[24] Z. Shi, R. Cao, K. Khan, A. K. Tareen, X. Liu, W. Liang, Y. Zhang, C. Ma, Z. Guo, X. Luo, H. Zhang, *Nano-Micro Lett.* **2020**, *12*, 99.
[25] O. A. Balitskii, W. Jaegermann, *Mater. Chem. Phys.* **2006**, *97*, 98.
[26] H. Bando, K. Koizumi, Y. Oikawa, K. Daikohara, V. A. Kulbachinskii, H. Ozaki, *J. Phys.: Condens. Matter* **2000**, *12*, 5607.
[27] D. Wines, J. A. Kropp, G. Chaney, F. Ersan, C. Ataca, *Phys. Chem. Chem. Phys.* **2020**, *22*, 6727.
[28] J. S. Liu, S. C. Huan, Z. H. Liu, W. L. Liu, Z. T. Liu, X. L. Lu, Z. Huang, Z. C. Jiang, X. Wang, N. Yu, Z. Q. Zou, Y. F. Guo, D. W. Shen, *Phys. Rev.* **2020**, *4*, 114005.
[29] S. Lei, J. Lin, Y. Jia, M. Gray, A. Topp, G. Farahi, S. Klemenz, T. Gao, F. Rodolakis, J. L. McChesney, C. R. Ast, A. Yazdani, K. S. Burch, S. Wu, N. P. Ong, L. M. Schoop, *Sci. Adv.* **2020**, *6*, eaay6407.
[30] J. A. W. Straquadine, *Evolution of the charge density wave state in the rare-earth tritellurides under uniaxial stress and disorder*, Stanford University, Stanford, California **2020**.
[31] K. Yumigeta, Y. Attarde, J. Kopaczek, M. Y. Sayyad, Y. Shen, M. Blei, S. T. R. Moosavy, Y. Qin, S. Tongay, *APL Mater.* **2022**, *10*, 111112.
[32] V. M. Goldschmidt, *Geochemische Verteilungsgesetze der Elemente/5, Isomorphie und Polymorphie der Sesquioxyde. Die Lanthaniden- Kontraktion und ihre Konsequenzen/von V.M. Goldschmidt, T. Barth u. G. Lunde*, Dybwad In Komm, Kristiania **1925**.
[33] H. Zhao, M. T. Pettes, Y. Zheng, H. Htoon, *Nat. Commun.* **2021**, *12*, 6753.
[34] J. Susoma, L. Karvonen, A. Säynätjoki, S. Mehravar, R. A. Norwood, N. Peyghambarian, K. Kieu, H. Lipsanen, J. Riikonen, *Appl. Phys. Lett.* **2016**, *108*, 073103.
[35] C. Trainer, C. M. Yim, C. Heil, F. Giustino, D. Croitori, V. Tsurkan, A. Loidl, E. E. Rodriguez, C. Stock, P. Wahl, *Sci. Adv.* **2019**, *5*, eaav3478.
[36] Y. Wang, K. Wang, Y. Ma, M. Zhou, H. Wang, G. Liu, *J. Phys.: Condens. Matter* **2021**, *33*, 355403.
[37] B. E. Deal, A. S. Grove, *J. Appl. Phys.* **1965**, *36*, 3770.
[38] M. Seitz, A. G. Oliver, K. N. Raymond, *J. Am. Chem. Soc.* **2007**, *129*, 11153.
[39] Y. Liu, C. Fu, K. Xia, J. Yu, X. Zhao, H. Pan, C. Felser, T. Zhu, *Adv. Mater.* **2018**, *30*, 1800881.
[40] Y. Chen, P. Wang, M. Wu, J. Ma, S. Wen, X. Wu, G. Li, Y. Zhao, K. Wang, L. Zhang, L. Huang, W. Li, M. Huang, *Appl. Phys. Lett.* **2019**, *115*, 151905.

Supporting information for: Experimental and theoretical studies of the surface oxidation process of Rare-Earth Tritellurides

Jan Kopaczek[1,2 a)], Kentaro Yumigeta[1], Akram Ibrahim[3], Mohammed Y. Sayyad[1], Shantanu Sinha[1], Renee Sailus[1], Patrick Hays[1], Seyed Tohid Rajaei Moosavy[1], Sandhya Susarla[1], Can Ataca[3, a)], Robert Kudrawiec[2 a)], and Sefaattin Tongay[1 a)]

[1]*Materials Science and Engineering, School for Engineering of Matter, Transport and Energy, Arizona State University, Tempe, Arizona 85287, USA*

[2]*Department of Semiconductor Materials Engineering, Faculty of Fundamental Problems of Technology, Wroclaw University of Science and Technology,*

Wybrzeże Wyspiańskiego 27, 50-370 Wrocław, Poland

[3] *Department of Physics, University of Maryland-Baltimore County, Baltimore, Maryland, 21250, USA*

[a)] Corresponding author: jkopacze@asu.edu, ataca@umbc.edu, sefaattin.tongay@asu.edu

1. Detailed theory description

(a) DFT main computational details. To get insight into the oxidation process, we perform DFT calculations within the generalized gradient approximation (GGA) by Perdew, Burke, and Ernzerhof (PBE) using the projector augmented wave (PAW) pseudopotentials implemented in the plane wave Vienna Ab initio Simulation Package (VASP).[1, 2] It is very important to note that both pseudopotentials for lanthanides (that include f-electrons as core or valence) are tested for consistency of the results. It is observed that adsorption/binding/deformation/cohesive/formation energies are negligibly affected by whether the f-electrons are treated as core or valance. To account for dispersion interactions, we include long-range dispersion correction in the DFT+D2 formulation of Grimme.[3] Collinear spin-polarized calculations are adopted with plane waves basis cutoff at 600 eV. The integration on the first Brillouin zone is carried out on uniform Monkhorst–Pack meshes with a meshing density of $16 \times 1 \times 16$ k-points for unit cells and $4 \times 1 \times 4$ k-points for $3 \times 1 \times 3$ supercells of RTe_3 monolayers. The $3 \times 1 \times 3$ supercell results in separation distances of about 13.1 Å and 12.8 Å between the adsorbed molecules on top of the $LaTe_3$ and $HoTe_3$ monolayers, respectively. These distances are enough to avoid the interactions between the images of the adsorbed molecules. The electronic self-consistent loop is ended if the energy change is less than 10^{-5} eV. The Fermi surface is Gaussian smeared by 0.01 eV. To avoid interlayer interaction, the RTe_3 monolayers are separated by a 23 Å vacuum region. For structural relaxation calculations, the structures are fully relaxed (both lattice parameters and atomic positions are allowed to relax) until atomic forces are less than 0.02 eV/Å and stresses are less than 1 kbar. Dipole corrections are not included in any direction during the DFT simulations due to large simulation cell sizes and limited computational power.

The adsorption energy of either O_2 or H_2O on top of RTe_3, E_{ads}, is defined as,

$$E_{ads} = E_{RTe_3+O_2/H_2O} - E_{RTe_3} - E_{O_2/H_2O}$$

Where $E_{RTe_3+O_2/H_2O}$ is the total energy of the structure after adsorption of an O_2 or H_2O molecule, E_{RTe_3} is the total energy of the bare RTe_3 structure before adsorption (both $E_{RTe_3+O_2/H_2O}$ and E_{RTe_3} calculations are conducted using $3 \times 1 \times 3$ supercells.), and E_{O_2/H_2O} is the total energy of an isolated O_2 or H_2O molecule.

The binding energy of either O_2 or H_2O to RTe_3, E_{bind}, is defined as,

$$E_{bind} = E_{ads} - E_{deform},$$

$$E_{deform} = E_{RTe_3}^{deformed} - E_{RTe_3}$$

Where $E_{RTe_3}^{deformed}$ is the total energy of the bare supercell after deformation due to the oxidation reaction. E_{deform} is subtracted from E_{ads} in the chemisorption cases, to avoid the possible errors that could arise from the finite supercell size that can be small compared to the strain fields created by the intercalation of oxygen atoms under the Te sheet. Therefore, E_{bind} is used for chemisorption cases to represent bond strength. In physisorption cases, E_{bind} and E_{ads} are almost the same due to the negligible E_{deform}, hence E_{ads} is generally used for physisorption cases.

The charge transfer to an element of type X, ΔQ (X), where X = R, Te, O or H, is defined as,

$$\Delta Q(X) = \Sigma_{i \in X} (Q_i^{\text{after adsorption}} - Q_i^{\text{before adsorption}})$$

Where Q_i is the Bader charge of atom *i*, and the summation runs over all atoms of type X. Thus, positive $\Delta Q(X)$ refers to electron charge gain, where negative $\Delta Q(X)$ refers to electron charge loss.

The adsorption of both H_2O and O_2 molecules is examined on top of $3 \times 1 \times 3$ supercells of $LaTe_3$ and $HoTe_3$ monolayers at three high symmetry sites, as illustrated in Fig. S1. The molecules adsorption is examined in two orientations, parallel and vertical with respect to the monolayers.

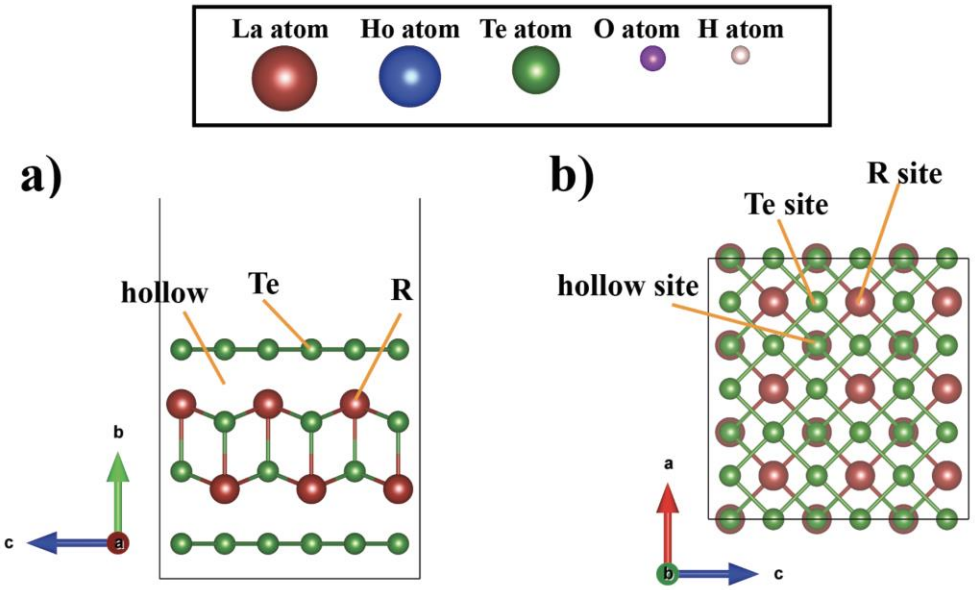

Fig. S1. Side and top views (**a** and **b**) of RTe_3 monolayer (only $LaTe_3$ is shown for clarity) with the high-symmetry sites on top of which H_2O and O_2 adsorptions are investigated. The upper box indicates the colors used to represent the different atom types discussed in the paper.

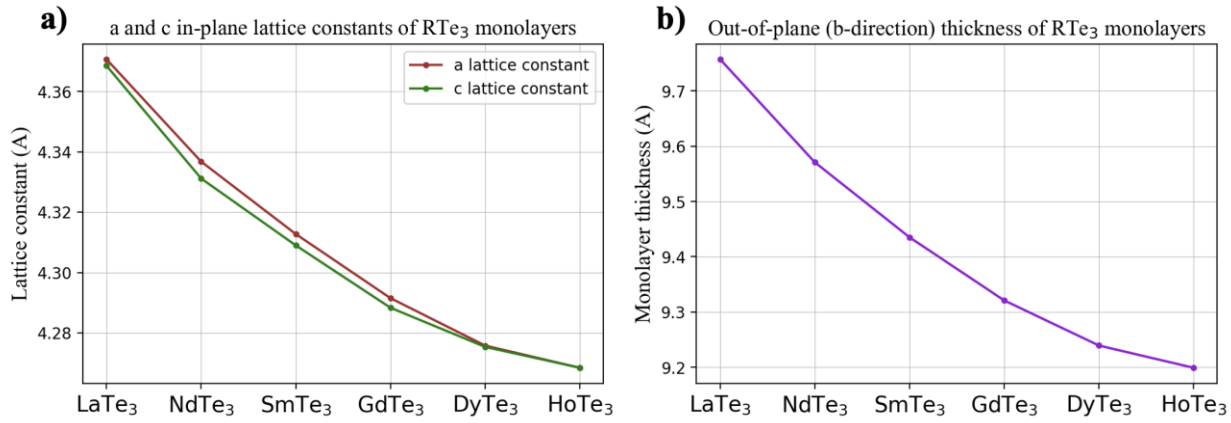

Fig. S2. (a) In-plane lattice constants, and (b) out-of-plane thickness (measured from top to bottom Te layers shown in Fig. S1(a)) of the considered RTe_3 monolayers after DFT structural relaxations.

(b) Cohesive energies and vacancy formation energies.

1. **The cohesive energy (eV/atom) for all RTe_3 monolayers are calculated as follows,**

$$E_{coh} = (E_{RTe_3} - n_R \times E_R - n_{Te} \times E_{Te})/(n_R + n_{Te})$$

Where E_{RTe_3}, E_R, and E_{Te} are the energies of the considered monolayer, isolated R atom, and isolated Te atom, respectively.

2. **<u>The Te vacancy formation energy (eV/Te vacancy) is calculated as follows,</u>**

$$E_{form}^{Te_{vac}} = (N_{Te}^{defects} \times E_{Te} + E_{RTe_3}^{defected} - E_{RTe_3})/N_{Te}^{defects}$$

Where E_{Te}, $E_{RTe_3}^{defected}$, and E_{RTe_3} are the energy of isolated Te atom (considered as Te chemical potential), energy of monolayer supercell defected by $N_{Te}^{defects}$ in the upper Te layer, and energy of the pristine supercell, respectively.

For single Te vacancy, we used $3 \times 1 \times 3$ supercells decorated by a single Te vacancy in the upper Te sheet to minimize vacancy interactions with its periodic images, in order to mimic the dilute vacancy concentrations observed in experimental reality.

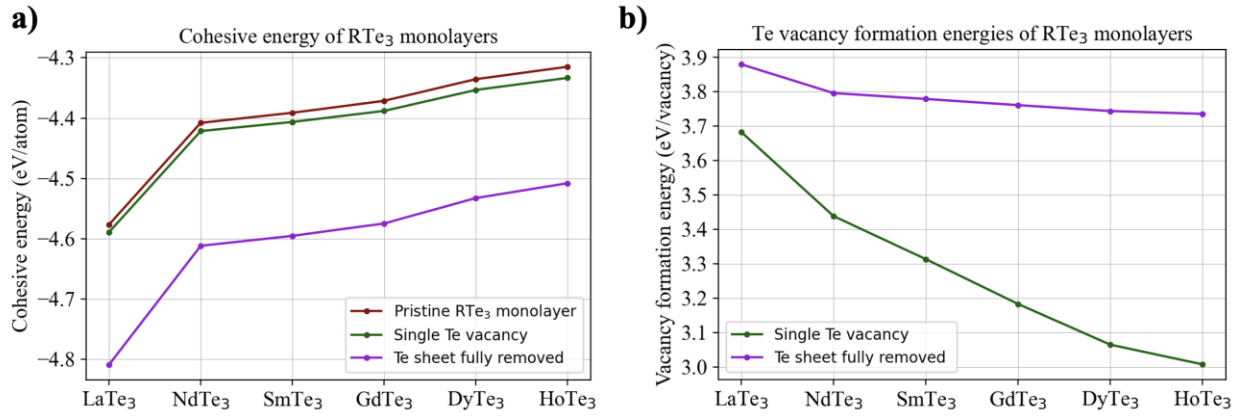

Fig. S3. (a) Cohesive energies of RTe_3 monolayers in three different cases (pristine monolayer, monolayer with one Te vacancy in the upper Te sheet, and monolayer with the upper Te sheet fully removed). (b) Te vacancy formation energies in 2 different cases (single Te vacancy, and full removal of upper Te sheet).

(c) Work functions of RTe_3 materials

Table S1. Work functions calculated for pristine and defective RTe_3 monolayers.		
RTe_3	**Pristine RTe_3**	**Defective RTe_3**
$LaTe_3$	4.891 eV	4.282 eV
$NdTe_3$	4.756 eV	4.112 eV
$SmTe_3$	4.700 eV	3.991 eV
$GdTe_3$	4.648 eV	3.913 eV
$DyTe_3$	4.614 eV	3.856 eV
$HoTe_3$	4.601 eV	3.825 eV

(d) Interaction between pristine RTe_3 monolayers and H_2O molecules. For H_2O, no dissociation is observed at any of the three sites including both parallel and vertical orientations of H_2O. We tried initializing the H_2O molecule at very close vertical distances to the surface to enforce any possible chemical adsorption, however, it always converges to a physisorption state in which the H_2O molecule is oriented perpendicular to the surface, with the two H atoms being closer to the surface as shown in Fig. S4. This orientation is due to the higher electronegativity of O with respect to H, which results in a gain of a slight negative charge around the O atom and a slight positive charge around the H atoms (see Fig. S5). This leads to the observed orientation in which the H atoms are closer to the Te surface and thus, the repulsion between the H_2O molecule and the surface electrons is lower. Table S2 tabulates the physisorption binding energy and charge transfer for each atom type. This behavior indicates that H_2O is not reactive on top of clean pristine RT_3 surfaces. The physisorption situation can be observed from the weak van der Waals binding energy and the small charge transfer as indicated in Table S2.

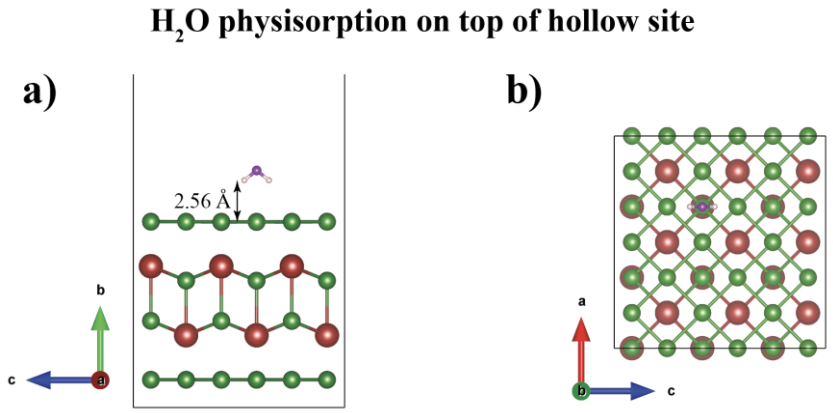

Fig. S4. Side and top views (**a** and **b**) of $LaTe_3$ monolayer with the physiosorbed H_2O molecule on top of the hollow site. Similar configurations are obtained for adsorption on top of the Te and R sites. Note that the same behavior occurs also for adsorption on top of the different sites of $HoTe_3$.

To illustrate the charge transfer process, two charge density difference plots for H_2O adsorption on top of the hollow sites of $LaTe_3$ and $HoTe_3$ are depicted in Fig. S5.

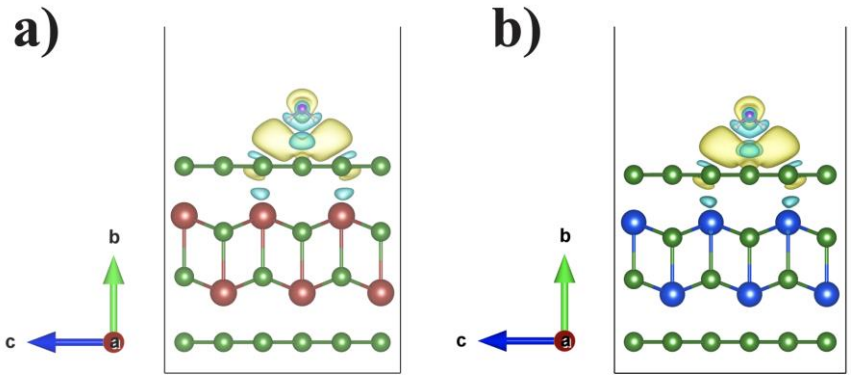

Fig. S5. Side views of the charge density difference plots of H_2O physisorption on top of the hollow sites of both $LaTe_3$ and $HoTe_3$ monolayers. The same illustrated behavior occurs also for adsorption on top of the Te and R sites. The yellow regions indicate charge accumulation, and the cyan ones indicate charge depletion. Isosurface values for charge accumulation and depletion are taken as 0.005 e/Å^3.

Table S2. Details of H_2O adsorption on top of $LaTe_3$ and $HoTe_3$. E_{ads} represents the adsorption energy and ΔQ represents the charge transfer to each atom type (obtained using Bader analysis.)

Structure	Site	E_{ads} (eV)	ΔQ (O)	ΔQ (H)	ΔQ (R)	ΔQ (Te)
$LaTe_3$	Te	-0.1175	0.033	-0.009	0.017	-0.041
	R	-0.1818	0.000	0.040	0.033	-0.073
	Hollow	-0.1825	0.000	0.042	0.025	-0.066
$HoTe_3$	Te	-0.0973	0.070	-0.057	-0.018	0.006
	R	-0.1879	0.072	-0.034	-0.030	-0.008
	Hollow	-0.1898	0.037	0.001	-0.073	0.034

(e) Interaction between RTe_3 monolayers and O_2 molecules. For the O_2 molecule to chemically adsorb to the surface, it first needs to possess enough energy to overcome the dissociation barrier and move from the molecular physisorption state to a dissociated state in which the atomic oxygen can chemically bind to the monolayer. Table S3 indicates the adsorption states O_2 can achieve at the different sites and orientations. Each site and orientation can have a state of O_2 physisorption, but the table denotes the most reactive state that O_2 can achieve at each site and orientation. The behavior shown in Table S3 is observed for both $LaTe_3$ and $HoTe_3$.

Table S3. Details about the most reactive state that O_2 can achieve at each site and orientation.

Site (orientation)	**Adsorption type**
Te (parallel)	Molecular chemisorption
Te (vertical)	Physisorption
R (parallel)	Dissociative chemisorption
R (vertical)	Dissociative chemisorption
Hollow (parallel)	Dissociative chemisorption
Hollow (vertical)	Dissociative chemisorption

Adsorption on top of Te with the O_2 molecule being vertically oriented always converges to a physisorption situation, while if it is oriented parallel to the surface, a molecular chemisorption can happen with a moderate charge transfer (~ 1.1 e^-) that leads to stretching the O-O bond length from 1.23 Å to around 1.58 Å, but without O_2 dissociation. We tried initializing the O_2 molecule at very close distances to the surface, but no dissociation takes place, which indicates the relatively high dissociation barrier on top of the Te site.

For the physisorption states, the physisorption situation can be observed from the weak van der Waals binding energy and the small charge transfer as indicated in Table S4. Fig. S6 illustrates the equilibrium physisorption configurations for adsorption on top of the R site of $LaTe_3$, as an example. Similar behavior is observed for adsorption on top of the hollow and Te sites as well. Only $LaTe_3$ is illustrated in Fig. S6 for clarity, but the same behavior is observed for $HoTe_3$.

Table S4. Details of O_2 physisorption on top of $LaTe_3$ and $HoTe_3$. E_{ads} represents the adsorption energy and ΔQ represents the Bader charge transfer to each atom type.

Structure	Site (orientation)	E_{ads} (eV)	ΔQ (O)	ΔQ (R)	ΔQ (Te)
$LaTe_3$	Te (parallel)	-0.073	0.022	0.034	-0.056
	Te (vertical)	-0.054	0.019	0.032	-0.050
	Hollow (parallel)	-0.108	0.062	0.042	-0.104
	Hollow (vertical)	-0.099	0.062	0.034	-0.096
	R (parallel)	-0.121	0.077	0.039	-0.115
	R (vertical)	-0.099	0.068	0.030	-0.098
$HoTe_3$	Te (parallel)	-0.089	0.055	-0.060	0.005
	Te (vertical)	-0.061	0.031	-0.012	-0.019
	Hollow (parallel)	-0.123	0.064	0.010	-0.074
	Hollow (vertical)	-0.111	0.078	0.011	-0.088
	R (parallel)	-0.139	0.098	-0.040	-0.058
	R (vertical)	-0.111	0.063	-0.038	-0.025

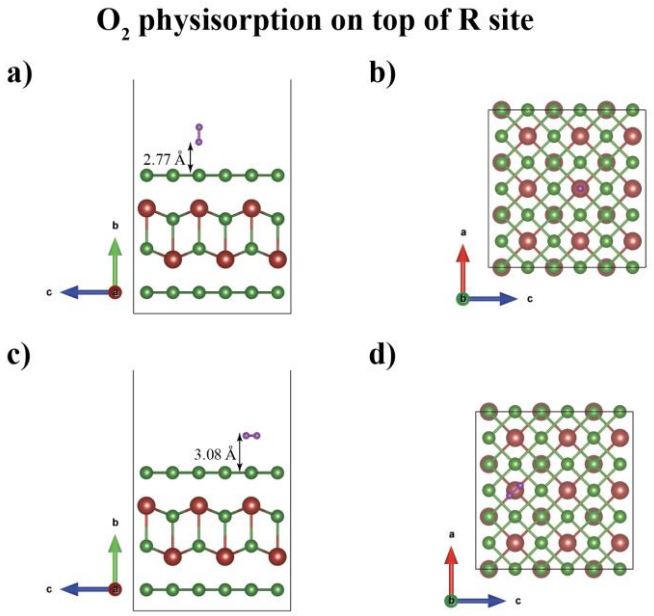

Fig. S6. Side and top views of $LaTe_3$ monolayers with the O_2 molecule physisorbed on top of the R site. Subfigures (**a** and **b)** and (**c** and **d**) denote the parallel and vertical orientations, respectively. The same illustrated behavior occurs also for $HoTe_3$.

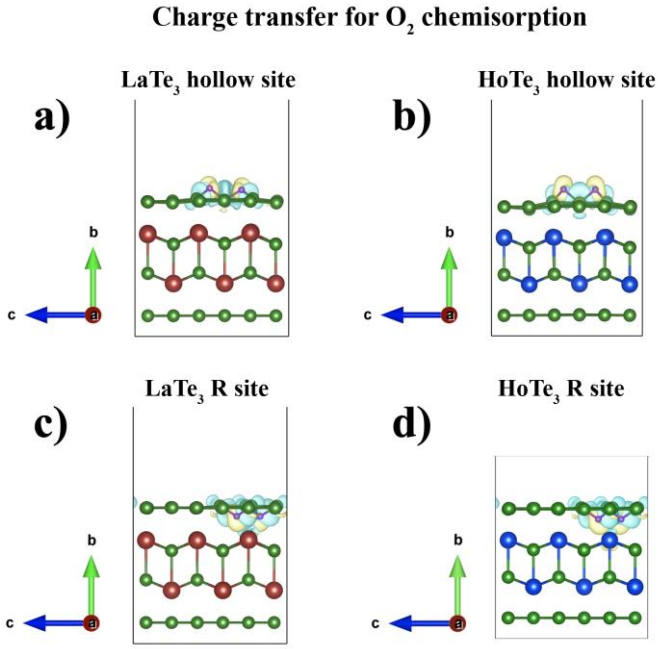

Fig. S7. Side views of the charge density difference plots of O_2 chemisorption on top of the hollow (**a** and **b**) and R sites (**c** and **d**) of both $LaTe_3$ and $HoTe_3$ monolayers (parallel orientation). The yellow regions indicate charge accumulation, and the cyan ones indicate charge depletion. Isosurface values for charge accumulation and depletion are taken as 0.004 e/Å^3.

(f) Estimation of the dissociation barriers of O_2 on top of RTe_3. We here discuss how the dissociation barriers and the associated threshold dissociation distances, d_{diss}, are obtained. For this, we place the O_2 molecule horizontally at the target site with variable vertical distance from the monolayer and then allow the O_2 molecule to relax in the horizontal plane only, until the atomic forces are less than 0.02 eV/Å. The atomic positions of RTe_3 are kept fixed through the simulation. Thus, we treat the monolayer as an effective potential acting on the O_2 molecule. Subplots (c) and (d) in Fig. S8-a, show the variation in O-O bond length as a function of the vertical distance from the surface. At the critical distance, we can observe a sudden jump in the O-O bond length which indicates dissociation. The corresponding interaction energies between the O_2 molecule and the RTe_3 surface are shown in subplots (a) and (b) in Fig. S8-a, where we can notice that the interaction energy reaches its maximum at the critical distance. The interaction energy at z vertical distance from the surface, $E_{int}(z)$, is calculated as follows,

$$E_{int}(z) = E_{RTe_3+O_2} - E_{RTe_3} - E_{O_2}(z)$$

Where $E_{RTe_3+O_2}$, E_{RTe_3}, and $E_{O_2}(z)$ are the energies of the total system at distance z, the energy of pristine RTe_3 monolayer, and the energy of an isolated oxygen molecule with its stretched bond experienced at the vertical distance z.

Note that the interaction energies are almost the same from the physisorption state up to the transition state due to the short-sightedness of 4f electrons that makes a negligible difference between $LaTe_3$ and $HoTe_3$ binding characteristics at the large distances. Close to the transition state, one can note that O_2 tends to dissociate earlier on top of $HoTe_3$. The smaller out-of-plane lattice constant of $HoTe_3$ leads to a shorter total distance between O_2 and lanthanide atoms for the same z from the surface, which results in a slightly higher impact on O-O bond stretch above $HoTe_3$ at the same vertical distance z, and thus slightly earlier dissociation. Nevertheless, the resultant difference in forward energy barrier (transition state energy – physisorption energy) is negligible. It is the reverse energy barrier (transition state energy – chemisorption energy) that makes the significant difference between different RTe_3 materials. As the number of 4f electrons increases, there exists a larger difference between chemisorption energy and transition state energy, leading to a higher reverse barrier, which results in a lower rate of desorption from the surface and thus, faster oxidation.

Estimated O_2 dissociation energy barriers:
Forward barrier energy = 1.8 eV for both pristine $LaTe_3$ and $HoTe_3$ at hollow and R sites

Reverse barrier energies (changes depend on the final chemisorption configuration as shown below):

O_2 above hollow site (horizontal)
$LaTe_3$: 2.7 eV, $HoTe_3$: 2.7 eV

O_2 above hollow site (vertical)
$LaTe_3$: 5.1 eV, $HoTe_3$: 5.4 eV

O_2 above R site (horizontal)
$LaTe_3$: 4.2 eV, $HoTe_3$: 4.3 eV

O_2 above R site (vertical)
$LaTe_3$: 6.0 eV, $HoTe_3$: 6.4 eV

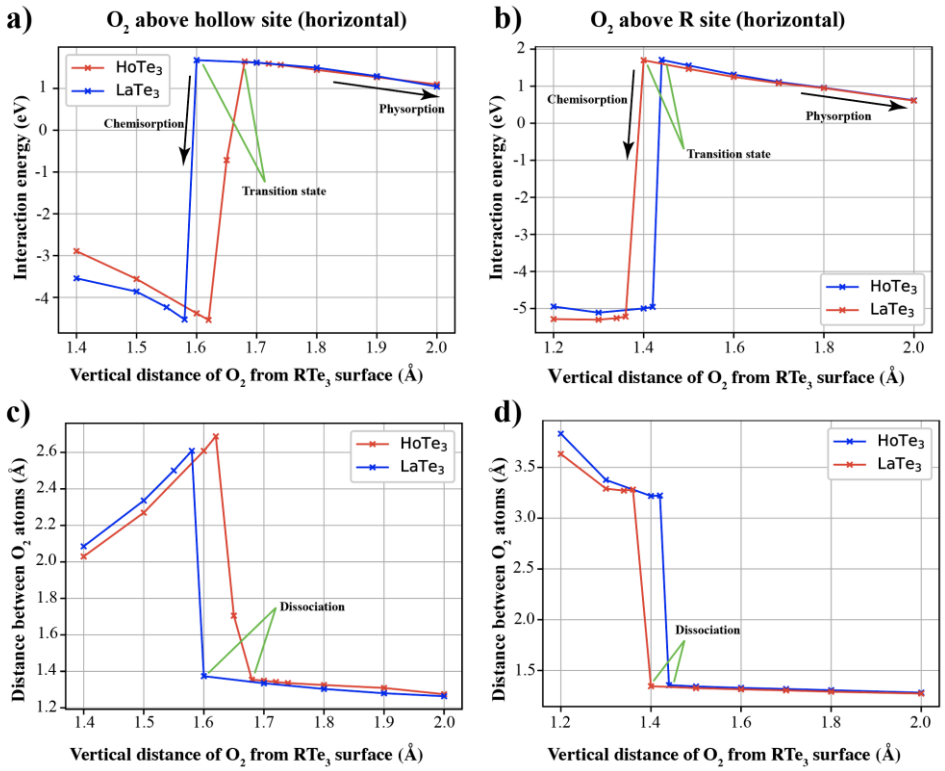

Fig. S8-a. The interaction energy between RTe_3 monolayer and O_2 molecule approaching its surface at the hollow and R sites (a and b). The O_2 bond length is also shown as a function of the vertical distance from the surface (c and d).

To estimate how strongly removing the upper Te sheet can affect the O_2 dissociation barrier, we calculated the interaction energy curve for a representative case of O_2 above defective $HoTe_3$. We found that the forward dissociation barrier reduces from 1.8 eV to 1.2 eV after the removal of the upper Te sheet.

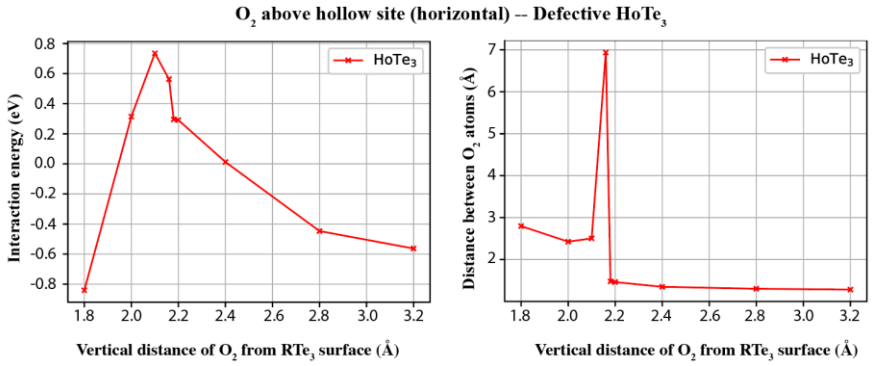

Fig. S8-b. The interaction energy between defective $HoTe_3$ monolayer and O_2 molecule approaching its surface at the hollow site. The O_2 bond length is also shown as a function of the vertical distance from the surface.

(g) A second barrier for subsurface adsorption. For most cases of dissociative adsorption, one or both of the oxygen atoms are observed to diffuse and bind to the subsurface (inner R-Te slab). Crossing the upper Te layer should be associated with a second energy barrier (other than the dissociation barrier). To have an idea of how large or small this barrier is, we try to estimate this barrier for the parallel O_2 adsorption case on top of the R site of $LaTe_3$, as an example. Generally, to have a second barrier, there must be a second local minimum above the Te surface other than the first local minimum which corresponds to the physisorption state. In this second local minimum, the dissociated O atoms are adsorbed above the Te surface. We first find this second local minimum by reducing the size of the relaxation step to avoid the diffusion of O atoms to the subsurface during relaxation. We find this second local minimum to have an adsorption energy of -0.149 eV, that is slightly lower than the physisorption state, which has an adsorption energy of -0.121 eV. We then try to estimate this second barrier of dissociated O atoms crossing the Te surface by having 7 images interpolated between the second local minimum and the final chemisorption state. The images are then relaxed while constraining the vertical positions of the O atoms (the lower 2 rows in RTe_3 monolayer were fixed as well). The estimated energy of this second barrier is 0.265 eV (see Fig. S9), which around 7 times smaller than the dissociation barrier energies.

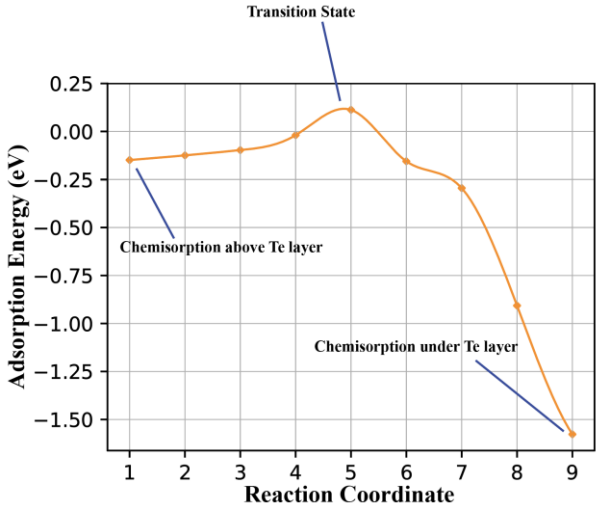

Fig. S9. The second barrier (for crossing the upper Te sheet) is shown for two oxygen atoms crossing the Te surface for the dissociative chemisorption case of O_2 on top of R site of $LaTe_3$ (parallel orientation) (see configuration (b) in Fig. 5). The energy of this barrier is estimated to be 0.265 eV.

(h) Oxidation behavior at surface topological defects. The prior DFT investigations demonstrate that the upper tellurium sheet can be acting as a solid barrier for the reactant molecules preventing them from reaching to the inner corrugated R-Te slab, where the reactant molecules can bind more strongly to the R atoms. However, from an experimental point of view, topological defects where the inner R-Te slab is directly exposed to the environment are likely to exist. For this purpose, we introduce here our DFT calculations for an artificial RTe_3 structure with the upper Te sheet fully removed to model such defects and their effects on the chemical stability.

First, the upper Te sheet is removed, and the structure is fully relaxed,. Fig. S10, depicts the relaxed geometries of the $LaTe_3$ and $HoTe_3$ monolayers upon the removal of the upper Te sheet. One can notice that the upper side of the corrugated R-Te slab converts from its zigzag shape toward being

a planar surface, after the removal of the Te sheet. The lower side of the inner R-Te slab where the lower Te sheet is still present, keeps its corrugated surface.

Note that for the new planar surface, we have a new set of high symmetry sites. The R site and the new hollow site. The R site is the same as before. The previously named 'Te site' disappears with the removal of the upper Te sheet. The new hollow site is just the previously named 'hollow site' for the pristine RTe_3, but it has moved up to the surface upon the removal of the Te sheet.

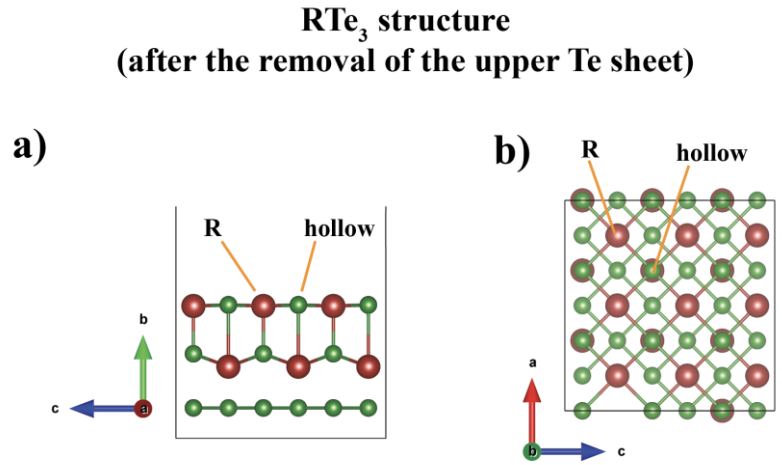

Fig. S10. Side and top views (**a** and **b**) of RTe_3 monolayer (only $LaTe_3$ is shown for clarity) with the high-symmetry sites on top of which H_2O and O_2 adsorptions are investigated. The zigzagged shape of the inner R-Te slab (see Fig. S1) relaxes here toward a flat layer.

For H_2O, we observe a dissociation to H^+ and OH^- above the hollow site (see Fig. S11), where the R site does not show a dissociative behavior. For the pristine RTe_3 structure, H_2O was not able to chemically adsorb to the RTe_3 material at any site, because of the repulsion between the negative charge on the O atom and the electrons of the Te sheet, which constituted a high energy barrier for H_2O chemisorption. Based on these results, H_2O can be considered as a probable cause of oxidation for defected regions where the preserving upper Te sheet does not exist.

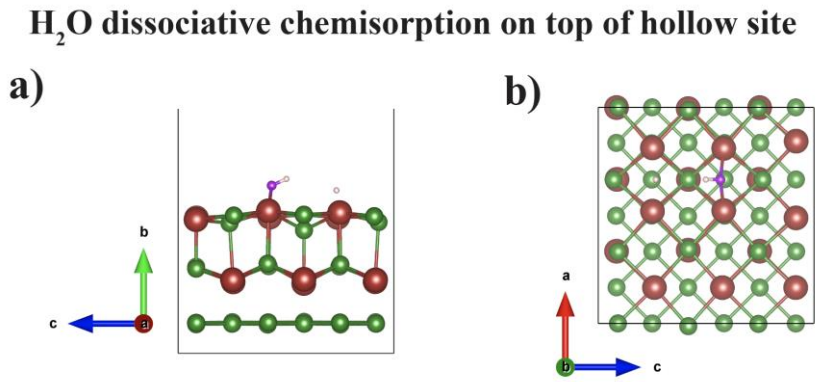

Fig. S11. Side and top views (**a** and **b**) of $LaTe_3$ monolayer with the chemisorped H_2O molecule on top of the hollow site after dissociation into H^+ and OH^-. Note that the same behavior occurs also for adsorption on top of the hollow site of $HoTe_3$.

For O_2, we have already observed its dissociative behavior even with the presence of the upper Te sheet. As should be expected, calculations for the defected RTe_3 structure show that O_2 can dissociate at both the new R and hollow sites. The O atoms are observed to migrate to the bridge sites, where each O atom binds to two R atoms (see Fig. S12).

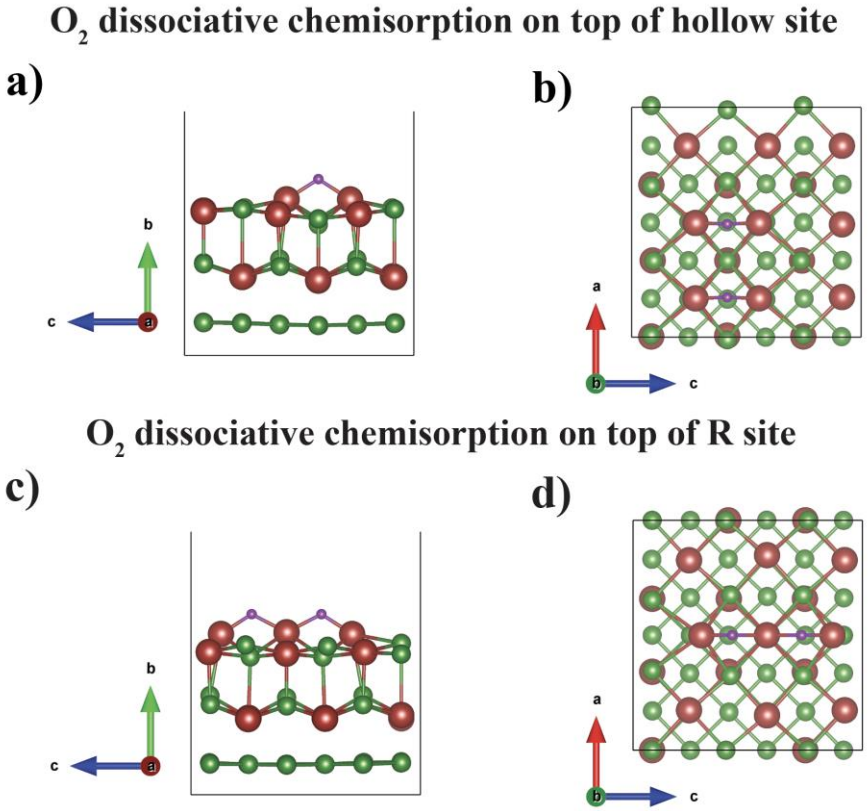

Fig. S12. Side and top views of O_2 dissociative chemisorption on top of hollow site (**a** and **b**) and R site (**c** and **d**) of $LaTe_3$ monolayer. Note that the same behavior occurs also for adsorption on top of the hollow and R sites of $HoTe_3$.

The above reported cases for O_2 chemisorption are found to occur when the O_2 molecule is initiated in a parallel orientation to the defected RTe_3 structure. Furthermore, we find that if an O_2 molecule approaches the R site in a vertical orientation, this can result in a molecular chemisorption situation (see Fig. S13), where one oxygen atom binds to the R atom and no dissociation takes place (only a stretch of the O-O bond is observed). A similar vertical orientation on the hollow site leads only to a physisorbed O_2 molecule. For the pristine RTe_3 with the presence of the upper Te sheet, molecular chemisorption of O_2 was always an endothermic reaction, however, after the Te sheet is removed, we notice that the molecular chemisorption of O_2 is now an exothermic reaction, which reflects its higher occurrence probability. This adds an extra possible channel of O_2 oxidation at the defective sites.

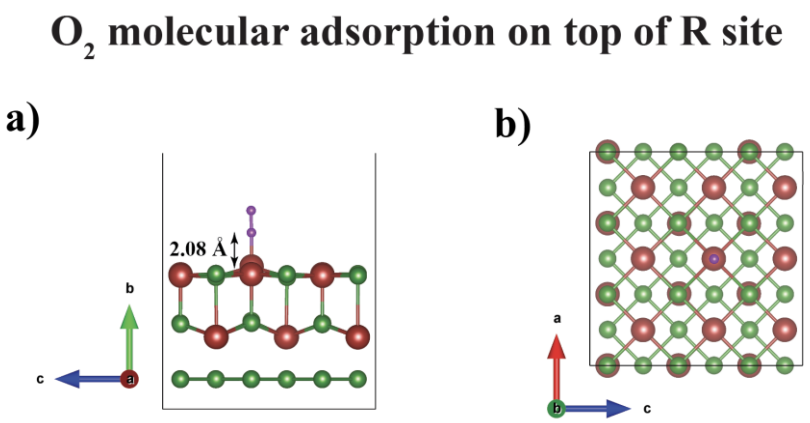

Fig. S13. Side and top views (**a** and **b**) of $LaTe_3$ monolayer with the chemisorped molecular O_2 (without dissociation) on top of the R site. Note that the same behavior occurs also for adsorption on top of the R site of $HoTe_3$.

2. Supporting information related to the experimental part of the article

2.1 Work function determination by KPFM (kelvin probe force microscopy):

To obtain the work function of pristine and oxidized $LaTe_3$ crystal, we have first measured by KPFM method HOPG (highly oriented pyrolytic graphite) exfoliated on GaAs substrate. Knowing the potential difference between HOPG and GaAs and also the work function of HOPG (4.475 eV[4]), we could determine the work function of GaAs substrate (~ 4.705 eV). Afterward, we prepared a $LaTe_3$ thin sheet (~ 20 nm) on the GaAs substrate from the same wafer and performed a KPFM scan before and after oxidation. Eventually, having the value of the work function for GaAs and a potential difference between $LaTe_3$ and the used substrate, we could calculate the work function of $LaTe_3$.

2.2 Results of XPS (X-ray photoelectron spectroscopy) measurements:

XPS measurements were performed in a high vacuum chamber (~ 10^{-9} Torr) using a non-monochromatic Al Kα X-ray source (1486.6 eV). The obtained results for freshly exfoliated and oxidized crystals are shown in fig. S11. For pristine $DyTe_3$ crystal, we have identified three peaks in the obtained XPS spectra, two of which are related to Te and one to Dy elements. The obtained binding energy for Te $3d_{3/2}$ and Te $3d_{5/2}$ closely resembles the commonly accepted value for non-oxidized Te, which is 573 and 583 eV, respectively.[5] After exposing the sample to ambient conditions for 4 hours, XPS spectra were collected again. It can be seen that for degraded crystal, new peaks emerged at 576.1 and 586.5 eV, which are related to TeO_2 and other Te oxide complexes.[5] Moreover, it is worth mentioning that the peaks related to the pristine sample are still visible, which suggests that some part of the crystal is non-oxidized and Te atoms are bonded to Dy.

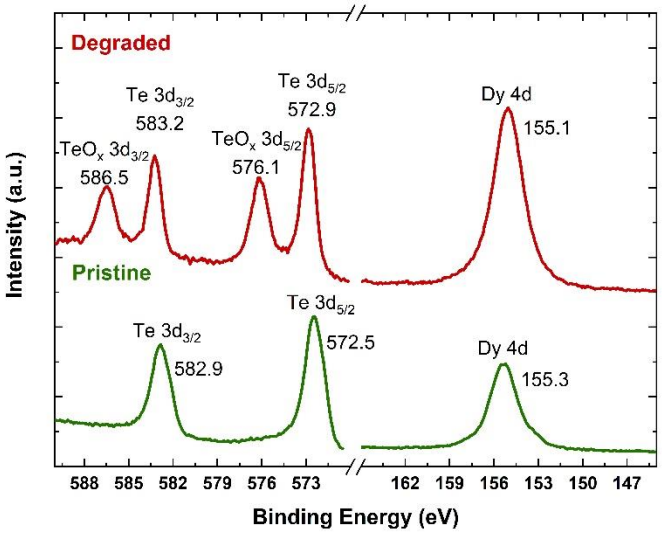

Fig. S14 XPS spectra for pristine (green line) and oxidized (red line) $DyTe_3$ crystals.

2.3 In-situ Raman spectroscopy and kinetics of the reaction for $NdTe_3$, $SmTe_3$, $GdTe_3$, $DyTe_3$, and $HoTe_3$:

Below, we have included the results of Raman spectra measurements with the time of oxidation and analysis of the RTe_3/TeO_x integrated intensity ratio for the remaining crystals considered in our studies and not included in the main article.

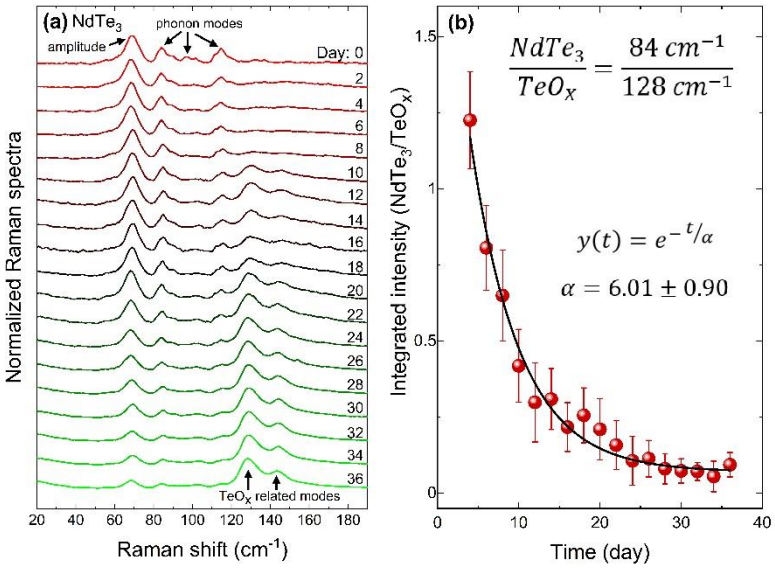

Fig. S15 Time-dependent Raman studies of the kinetics of oxidation of $NdTe_3$ material. (a) Raman spectra of $NdTe_3$ crystal were obtained as time progressed from 0 to 36 days. (b) The time-dependent ratio of the integrated intensity of one of the $NdTe_3$ vibrational modes (84 cm^{-1}) and TeO_x (128 cm^{-1}) oxidation peaks. The black line represents fitting with an exponential function.

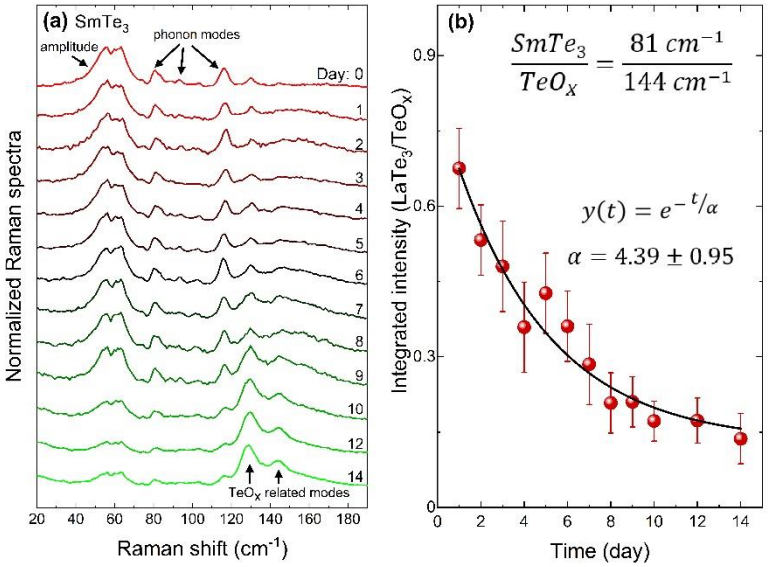

Fig. S16 Time-dependent Raman studies of the kinetics of oxidation of $SmTe_3$ material. (a) Raman spectra of $SmTe_3$ crystal were obtained as time progressed from 0 to 14 days. (b) The time-dependent ratio of the integrated intensity of one of the $SmTe_3$ vibrational modes (81 cm^{-1}) and TeO_x (144 cm^{-1}) oxidation peaks. The black line represents fitting with an exponential function.

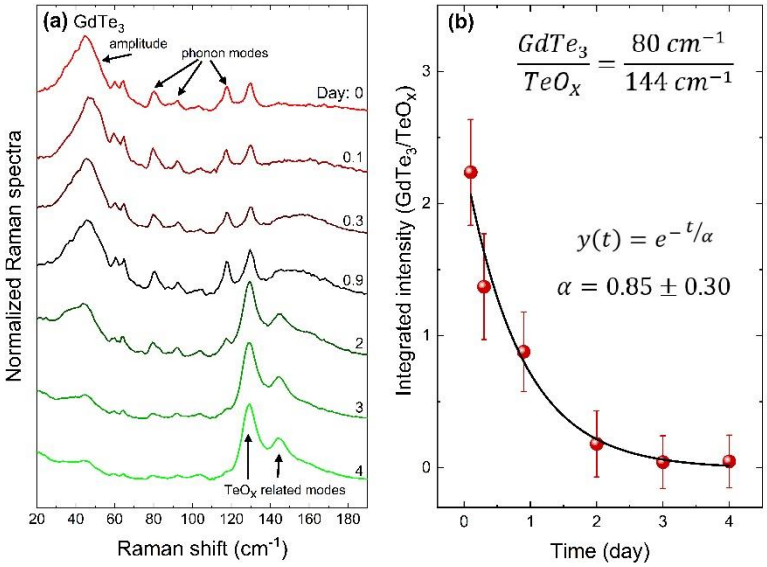

Fig. S17 Time-dependent Raman studies of the kinetics of oxidation of $GdTe_3$ material. (a) Raman spectra of $GdTe_3$ crystal were obtained as time progressed from 0 to 4 days. (b) The time-dependent ratio of the integrated intensity of one of the $GdTe_3$ vibrational modes (80 cm^{-1}) and TeO_x (144 cm^{-1}) oxidation peaks. The black line represents fitting with an exponential function.

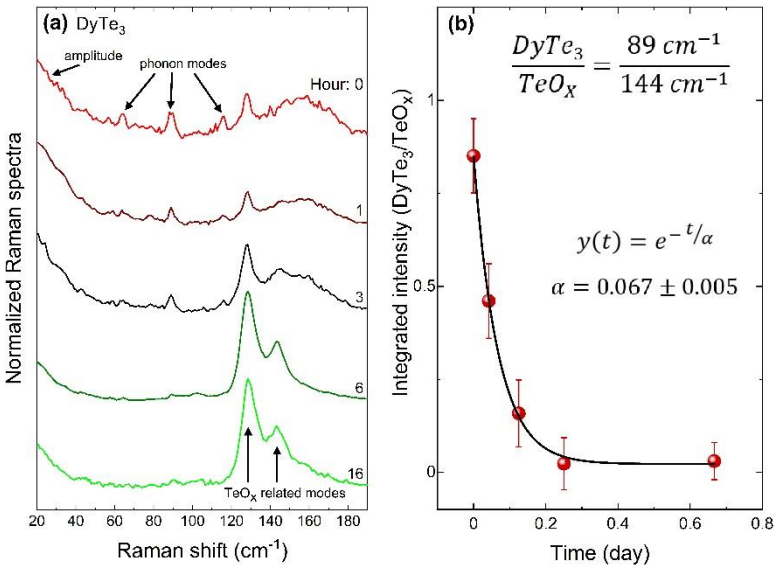

Fig. S18 Time-dependent Raman studies of the kinetics of oxidation of $DyTe_3$ material. (a) Raman spectra of $DyTe_3$ crystal were obtained as time progressed from 0 to 16 hours. (b) The time-dependent ratio of the integrated intensity of one of the $DyTe_3$ vibrational modes (89 cm^{-1}) and TeO_x (144 cm^{-1}) oxidation peaks. The black line represents fitting with an exponential function.

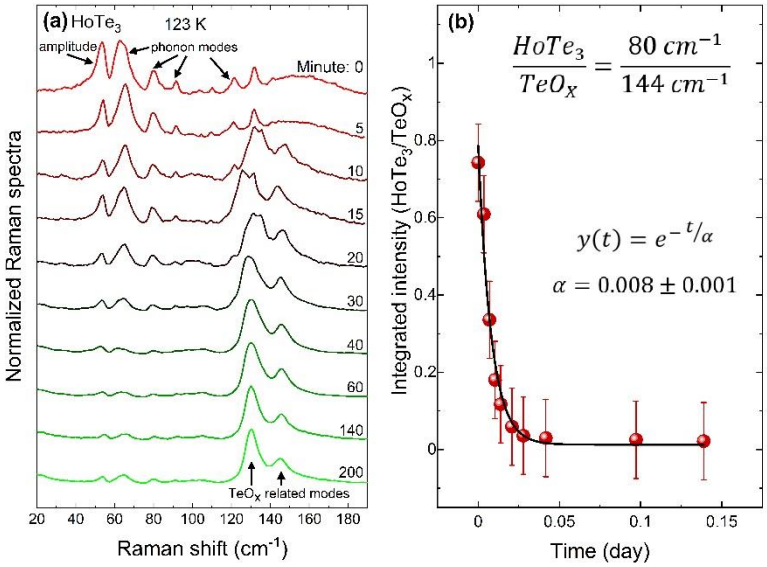

Fig. S19 Time-dependent Raman studies of the kinetics of oxidation of $HoTe_3$ material. (a) Raman spectra of $HoTe_3$ crystal were obtained as time progressed from 0 to 200 minutes. Moreover, all the spectra were collected at 123 K due to the low intensity of Raman modes at room temperature. (b) The time-dependent ratio of the integrated intensity of one of the $HoTe_3$ vibrational modes (80 cm^{-1}) and TeO_x (144 cm^{-1}) oxidation peaks. The black line represents fitting with an exponential function.

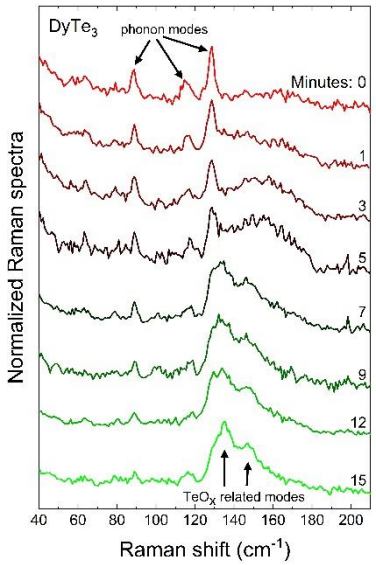

Fig. S20 Raman spectra of $DyTe_3$ crystal immersed in the water showing that H_2O also leads to oxidation.

(1) Kresse, G.; Furthmuller, J. Efficient iterative schemes for ab initio total-energy calculations using a plane-wave basis set. Phys. Rev. B 1996, 54, 11169−11186.
(2) Perdew, J. P.; Burke, K.; Ernzerhof, M. Generalized Gradient Approximation Made Simple. Phys. Rev. Lett. 1996, 77, 3865−3868.
(3) Grimme, S. Semiempirical GGA-type density functional constructed with a long-range dispersion correction. J. Comput. Chem. 2006, 27, 1787−1799.

(4) Hansen W. N.; Hansen G. J. Standard reference surfaces for work function measurements in air. Surface Science 2001, 481, 172–184.
(5) Handbook of X-ray Photoelectron Spectroscopy C. D. Wanger, W. M. Riggs, L. E. Davis, J. F. Moulder and G. E.Muilenberg Perkin-Elmer Corp., Physical Electronics Division, Eden Prairie, Minnesota, USA, 1979. 190 pp.